

# Seismotectonic significance of the 2008–2010 Walloon Brabant seismic swarm in the Brabant Massif, Belgium



Koen Van Noten<sup>a,\*</sup>, Thomas Lecocq<sup>a</sup>, Anjana K. Shah<sup>b</sup>, Thierry Camelbeek<sup>a</sup>

<sup>a</sup> Seismology-Gravimetry, Royal Observatory of Belgium, Ringlaan 3, 1180 Brussels, Belgium

<sup>b</sup> U.S. Geological Survey, P.O. Box 25046, Denver Federal Center, MS 964, Denver, CO 80225, USA

## ARTICLE INFO

### Article history:

Received 21 February 2015

Received in revised form 26 May 2015

Accepted 30 May 2015

Available online 14 June 2015

### Keywords:

Earthquake sequence

Intraplate seismicity

Relocation

Cross-correlation

Aeromagnetic matched filtering

Asquepont detachment fault

## ABSTRACT

Between 12 July 2008 and 18 January 2010 a seismic swarm occurred close to the town of Court-Saint-Etienne, 20 km SE of Brussels (Belgium). The Belgian network and a temporary seismic network covering the epicentral area established a seismic catalogue in which magnitude varies between  $M_L$  -0.7 and  $M_L$  3.2. Based on waveform cross-correlation of co-located earthquakes, the spatial distribution of the hypocentre locations was improved considerably and shows a dense cluster displaying a 200 m-wide, 1.5-km long, NW-SE oriented fault structure at a depth range between 5 and 7 km, located in the Cambrian basement rocks of the Lower Palaeozoic Anglo-Brabant Massif. Waveform comparison of the largest events of the 2008–2010 swarm with an  $M_L$  4.0 event that occurred during swarm activity between 1953 and 1957 in the same region shows similar P- and S-wave arrivals at the Belgian Uccle seismic station. The geometry depicted by the hypocentral distribution is consistent with a nearly vertical, left-lateral strike-slip fault taking place in a current local WNW–ESE oriented local maximum horizontal stress field. To determine a relevant tectonic structure, a systematic matched filtering approach of aeromagnetic data, which can approximately locate isolated anomalies associated with hypocentral depths, has been applied. Matched filtering shows that the 2008–2010 seismic swarm occurred along a limited-sized fault which is situated in slaty, low-magnetic rocks of the Mousty Formation. The fault is bordered at both ends with obliquely oriented magnetic gradients. Whereas the NW end of the fault is structurally controlled, its SE end is controlled by a magnetic gradient representing an early-orogenic detachment fault separating the low-magnetic slaty Mousty Formation from the high-magnetic Tubize Formation. The seismic swarm is therefore interpreted as a sinistral reactivation of an inherited NW–SE oriented isolated fault in a weakened crust within the Cambrian core of the Brabant Massif.

© 2015 Elsevier B.V. All rights reserved.

## 1. Introduction

Earthquake swarms or seismic swarms are defined as episodic sequences of a large number of seismic events that are clustered in space and time (Mogi, 1963). In contrast to a classical foreshock–mainshock–aftershock sequence, in which aftershock sequences may consist of numerous lower-magnitude earthquakes, seismic swarms are not marked by one single dominant event. The time history of a swarm is characterised rather by a gradual increase, or sometimes by a burst, of microseismic activity alternating with periods of low seismic rate or seismic quiescence. Sometimes dominant earthquakes may reach larger magnitudes during the course of a seismic swarm. The many small events in a seismic swarm can, however, often not be linked to an identifiable mainshock. This can result from a heterogeneous stress field in a weakened crust that lacks a single well-defined fault

structure. If such a fault structure were present, it might be capable releasing higher strain resulting in a higher magnitude earthquake (Fischer et al., 2014; Mogi, 1963). To precisely relocate the numerous events within a seismic sequence, it is necessary to analyse waveform data that are recorded by a dense local seismic network close to the epicentre of an earthquake swarm, allowing the detection of a large number of small events.

In an intraplate continental tectonic setting, seismic swarms are commonly associated with stress perturbations caused by magmatic intrusions, volcanic activity and with gradual fluid transport in the seismogenic part of the crust (Hainzl, 2004; Hiemer et al., 2012; Schenk et al., 2012; Špičák, 2000). In volcanic areas, continental rift and subduction zones, large fluid- and gas movements such as CO<sub>2</sub> release along prominent faults or fault intersections can generate earthquake swarms (e.g. Ibs-von Seht et al., 2008; Lindenfeld et al., 2012). Within the Eurasian tectonic plate, far away from any plate boundary, intense geothermal seismic swarms occur for example in the French/Italian Alps (e.g. Barani et al., 2014; Daniel et al., 2011; Leclère et al., 2012) or in the West Bohemia/Vogtland area in the Eger rift zone (e.g. Fischer et al., 2014; Parotidis et al., 2003; Schenk et al.,

\* Corresponding author. Tel.: +32 2 790 39 18.

E-mail addresses: [koen.vannoten@seismology.be](mailto:koen.vannoten@seismology.be) (K. Van Noten), [thomas.lecocq@seismology.be](mailto:thomas.lecocq@seismology.be) (T. Lecocq), [ashah@usgs.gov](mailto:ashah@usgs.gov) (A.K. Shah), [thierry.camelbeek@oma.be](mailto:thierry.camelbeek@oma.be) (T. Camelbeek).

2012). In these cases, the presence of suprahydrostatic overpressured fluids rising along a fault zone is often considered to trigger fault activity due to pore pressure changes, even when the fault is unfavourably oriented for reactivation (Leclère et al., 2012; Sibson, 1985) and especially if the crust is in a critical state (Parotidis et al., 2003).

Between 2008 and 2010, a seismic swarm occurred in the central part of Belgium in the basement rocks of the Lower Palaeozoic Anglo-Brabant Massif, here further referred to as the Brabant Massif. Although the studied 2008–2010 Walloon Brabant seismic sequence resembles other seismic swarms in terms of its temporal evolution, the lack of a main shock and the restricted spatial distribution, the Brabant Massif is not associated with any of the volcanic, geothermal or tectonic settings described above, nor is any induced seismicity going on. Although the seismicity within the seismotectonic zone of the Brabant Massif is considered as to be rather moderate, still a few of the largest (historical) earthquakes in Western Europe have occurred within this slate belt demonstrating its importance (Camelbeek et al., 2007). Linking these historical large earthquakes to potential individual fault structures has been difficult in the past, because of a lack of aftershocks and due to the limited seismic network. The rapid installation of a local network in the epicentral area of the 2008–2010 seismic swarm, however, allows us to study for the first time an extremely well documented seismic event in the old geological structure of the Brabant Massif.

The aim of this study is to investigate the specific geological structure that the swarm took place on. First, the hypocentre location is improved by the cross-correlation of waveforms of co-located events. A 3D analysis of the relocated hypocentre distribution delineates the dimension of the structure and frames the seismic sequence within the tectonic structure of the Brabant Massif. Second, stress inversion of the focal mechanisms of the largest-magnitude events is performed, allowing derivation of a best-fitting stress tensor and discussion of its correspondence to the regional stress field in northwestern Europe. Third, waveforms of the largest earthquakes are compared to analogue waveforms of a 1953 seismic event that belongs to a seismic swarm that occurred between 1953 and 1957 at Court-Saint-Etienne in the general same epicentral area as the 2008–2010 swarm. Finally, using the orientation of the seismic swarm, we attempt to link the fault structure to a relevant tectonic structure via aeromagnetic data. These data are matched-filtered to isolate anomalies that are likely to be due to sources at depths of interest. Such structures are of interest as they can play an important role accommodating deformation in a current stress field.

## 2. Geological and seismological settings

### 2.1. Regional setting

The study area is located in Belgium in NW Europe, more than 1000 km away from the boundaries of the Eurasian plate. The 2008–2010 Walloon Brabant seismic sequence occurred within the Lower Palaeozoic Brabant Massif, a slate belt situated in the subsurface of the central and northern part of Belgium. Outcrops of the Brabant Massif are sparse and are only present in some incised river valleys along the southern rim of the Brabant Massif. The Brabant Massif dips towards the north and is mostly covered by Cretaceous chalk, Cenozoic sand and clays, and Quaternary loess sediments. Well data indicates that the thickness of the cover rapidly increases to 1000 m at the Belgium–Dutch border (Legrand, 1968). Not much is known about the current deformation in the Brabant Massif, but incised river outcrops suggest uplift of the southern part and gradual deepening of its northern part. To the West, the Brabant Massif laterally extends towards the United Kingdom forming part of the larger tectonic unit of the Anglo-Brabant deformation belt (Verniers et al., 2002) (Fig. 1). To the east, it has been traced using borehole data and geophysical data beneath the thick Devonian and Carboniferous sequences of the Campine Basin (Figs. 1 and 2), as far as to the seismically active Lower Rhine

Embayment (Mansy et al., 1999). At its southern border, it is unconformably overlain by undeformed Middle Devonian deposits of the Brabant parautochthon (white area between Brabant Massif and Ardenne allochthon in Fig. 1). Further to the south, the Brabant parautochthon is tectonically overthrust by the Variscan Ardenne allochthon along the Midi–Aachen thrust, i.e. the Variscan front of the Rhenohercynian Zone (Fig. 1), during the late stage of the Variscan Orogeny in the Late Carboniferous. Because of its crystalline rigidity, the Brabant Massif acted as a backstop during the Variscan deformation resulting in oroclinal bending of the Palaeozoic deposits of the Ardenne allochthon (Van Noten et al., 2012).

### 2.2. Structural grain of the Brabant Massif

The structure of the Brabant Massif resulted from the ~30 Ma long-lasting, Acadian, Brabantian Deformation event that took place between the late Llandovery (c. 430 Ma) and Emsian (c. 400 Ma) (Debacker et al., 2005; Sintubin et al., 2009). As indicated on lithostratigraphic subcrop maps (Fig. 2a), the Brabant Massif has an apparent symmetrical geometry with a central Cambrian metasedimentary core flanked at both sides by Ordovician and Silurian metasedimentary rocks (De Vos et al., 1993b; Legrand, 1968; Piesens et al., 2005). Structural field work, gravimetric and aeromagnetic anomaly maps (Fig. 2c) show that the Brabant Massif has a dominant NW–SE trending structural grain that curves into a ENE–WSW orientation towards the east. Owing to the high magnetic susceptibility of the rock formations (slate, siltstone, metasandstone, metagreywacke) of the Lower Cambrian Tubize Group, the Cambrian core is clearly visible on the aeromagnetic anomaly map (Chacksfield et al., 1993; Sintubin, 1999). In contrast, the Bouguer gravity anomaly (Fig. 2b) shows the opposite pattern, with positive anomalies related to the Ordovician–Silurian rim and gravity lows associated with the Cambrian core or other deep-seated bodies (Everaerts and De Vos, 2012; Piesens et al., 2005). The arcuate geometry of fold-and-cleavage patterns inferred from potential-field data throughout the slate belt illustrates the change in orientation of the structural grain from west to east (Sintubin, 1999; Sintubin et al., 2009). Tectonic inversion of the Cambrian to Silurian Brabant Basin resulted in the formation of a steep compressional wedge in which the Cambrian core is strongly deformed and is covered by a less deformed Ordovician–Silurian at its peripheral domains. The decrease in deformation from the core to the peripheral domain is characterised by a decrease in metamorphic grade towards the Silurian flanks of the Brabant Massif and by a change of a steep fold belt in the central part to a rather wide and open fold belt in the peripheral part. The SW boundary of the Brabant Massif corresponds with a steep east–west oriented gravity gradient on the Bouguer anomaly map and the highest relief and most prominent magnetic highs on the aeromagnetic anomaly map. *La Bordière fault* defines the southern limit of the Brabant Massif and coincides with a sharp gravimetric anomaly gradient (Legrand, 1968) (Fig. 2b) juxtaposing the dense rocks of the Brabant Massif from less dense Upper Palaeozoic rocks of southern Belgium (Chacksfield et al., 1993).

In the SW part of the Brabant Massif, several NW–SE trending Bouguer anomaly gravity lows (indicated as gl in Fig. 2b) are interpreted as low-density crystalline basement at a minimum depth of 2.5 km (Everaerts et al., 1996; Lee et al., 1993). The NNE–SSW shortening and arcuate shape of the Brabant Massif is believed to be caused by the compression of the Cambrian core of the slate belt against these low-density bodies. This compression led to the lateral tectonic escape of the Cambrian core along dextral transpressional shear zones. These shear zones are interpreted as Palaeozoic NW–SE strike-slip faults as they coincide with several of the NW–SE trending aeromagnetic gradient lineaments shown in Fig. 2c and are also seen as Bouguer gravity gradients (dashed lines in Fig. 2b) (Everaerts and De Vos, 2012; Sintubin, 1999; Sintubin and Everaerts, 2002). Detailed stratigraphic and structural work, however, revealed that these shear zones

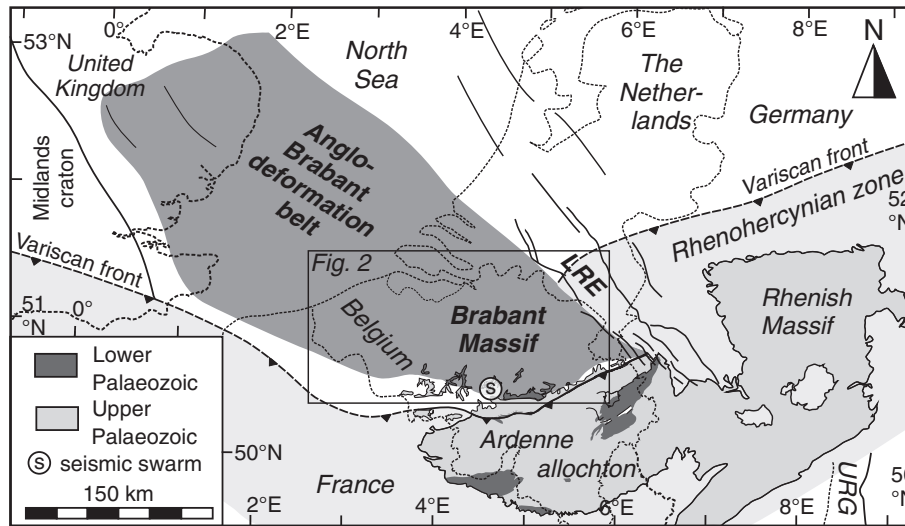


**Fig. 1.** Intraplate tectonic setting of the Brabant Massif. The Brabant Massif forms part of the Anglo-Brabant deformation belt that extends from central and north Belgium to the south-eastern part of the UK. The seismic swarm is situated at the southern border of the Brabant Massif. The Brabant Massif is partly overthrust in the south by the Ardenne allochthon along the Midi–Aachen thrust, i.e. the Variscan front of the Rhenohercynian zone. Deposits of the Rhenohercynian zone are exposed in the Ardenne allochthon and Rhenish Massif. LRE: Lower Rhine Embayment; URG: Upper Rhine Graben. Tectonic terrains after Sintubin et al., 2009 and Verniers et al., 2002.

are blind structures that do not reach the present-day erosion surface of the Brabant basement. The only structural indicators of these shear zones at the surface are short and local transitions of steeply- to gently plunging folds (Debacker, 2012; Debacker et al., 2003; Debacker et al., 2004a; Debacker et al., 2004b).

### 2.3. Historical seismicity in the Brabant Massif

Seismicity within the seismotectonic zone of the Brabant Massif is considered low to moderate (Camelbeeck et al., 2007; Leynaud et al., 2000). The largest onshore historical event on the Belgian territory was the 11 June 1938 earthquake ( $M_s = 5.0$ ) that occurred in the Brabant Massif at Zulzeke–Nukerke, near Oudenaarde (Fig. 2c). Reported damage (Somville, 1939) was primarily in an E–W oriented area surrounding that earthquake. The damage distribution was attributed to the site effects associated with soft-sediments overlying the Brabant Massif (Camelbeeck et al., 2014; Nguyen et al., 2004). Another significant event was the 20 June 1995 earthquake near Le Roeulx ( $M_L = 4.5$ ,  $M_s = 4.3$ ) at a depth of 24 km. Other historical earthquakes that occurred before the installation of the current Belgian permanent network and which caused considerable damage in the Brabant Massif are the 23 February 1828 ( $4.5 < M_L < 5.0$ ;  $M_s \sim 4.6$ ) near Jauche (Tienen) and the 21 May 1382 ( $M_s$  6.0) and 23 April 1449 ( $M_s$  5.5) events in the North Sea (Fig. 2c) (Melville et al., 1996), which are rather poorly-located by macroseismic analysis.

Between 1953 and 1957 a seismic sequence took place a few kilometres south of Court-Saint-Etienne, in a similar region as the 2008–2010 sequence. Only the largest events of this sequence were recorded by the Uccle seismic station (UCCS in Fig. 3), which was at that time the only operational station in Belgium. A comparison between the 1953 event of the 1953–1957 sequence and the 2008–2010 sequence is discussed in section 4.

## 3. Spatiotemporal seismic analysis

### 3.1. Temporary network and time history of seismicity

The Brabant Walloon seismic swarm started on 12 July 2008 with a  $M_L$  2.2 earthquake at a depth of 6.3 km. It was followed the day after by a  $M_L$  3.2 earthquake at 7.74 km depth, the largest earthquake in this seismic sequence. The day after the  $M_L$  3.2 earthquake, the first

two temporary stations were installed, followed by another 5 stations between 11 and 14 August 2008. This temporary network was deployed in the Court-Saint-Etienne–Ottignies area in a 10 km radius around the epicentres. Installation of the temporary network allowed the recording of very small events that could not be detected by distant stations and allowed excellent relocation of all events. The local 7-station network was operational between 14 August 2008 and 6 August 2010. It consisted of 4 short period LE-3D/5 s Lennartz seismometers and 3 CMG-3ESPC broadband Güralp seismometers that were installed in the hamlets of Grand Leez (GRZ), Mellery (OT1), Rixensart (OT2), Dion-le-Mont (OT3), Limal (OT4), Genappe (OT5) and Ottignies (OTT) (Table 1, Fig. 3). After the removal of the temporary network, a permanent station was installed on 13 July 2010 in Court-Saint-Etienne (CSE) to monitor the area continuously. The closest other active permanent stations are the Uccle (UCCS, UCCB), Seneffe (SNF), Ronquières (RNQ) and Steenkerque (SKQ) stations (Table 1, Fig. 3).

P- and S-wave arrival times were manually picked on a daily basis. Based on the time difference between P- and S-wave arrivals, amplitude and period measurements, a local magnitude  $M_L$  was estimated for each individual event. Earthquake magnitudes of the Walloon Brabant seismic swarm range randomly from  $M_L - 0.7$  to  $M_L$  3.2 without any clear relationship between earthquake magnitude and the time history of seismicity (Fig. 4). Such absence of correlation between earthquake magnitude and time history of events is typical for seismic swarms (Mogi, 1963) although higher magnitude earthquakes are often detected at the onset of a seismic swarm (e.g. in West-Bohemia, Fischer et al., 2014).

The time history of seismicity of the 239 recorded events shows that the seismic sequence can be subdivided in several periods of seismic activity alternating by periods of seismic quiescence (Fig. 4). A first large swarm (109 events) took place in the summer and autumn of 2008. After inactivity during 51 days the swarm shortly revived between 20 and 29 December 2008 (11 events). A second large swarm took place in the spring of 2009 (119 events) during which the seismic rate increased to sometimes ten events per day. Subsequently, some single events occurred in the summer of 2009. A minor amount of activity was detected in December 2009 (5 events) and the sequence ended on 18 January 2010 (3 events), 1.5 year after it started. After that, the activity shortly revived by two  $M_L$  1.0 and  $M_L$  1.2 events on 30 January 2011 and a recent single  $M_L$  1.0 event on 10 January 2014. A full catalogue of all events with their timing, location (after

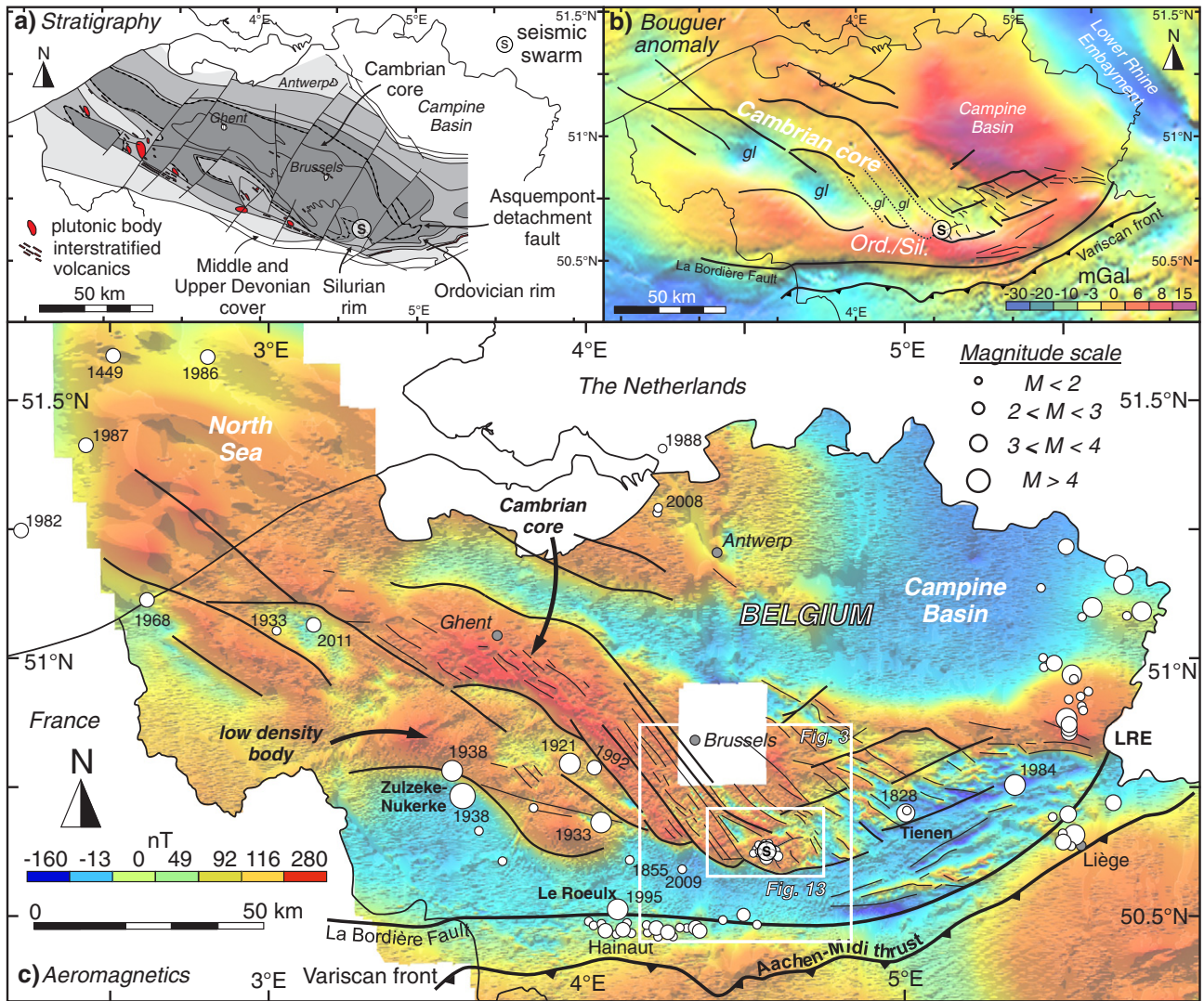


**Fig. 2.** a) Geological subcrop map and general stratigraphic structure of the Lower Palaeozoic Brabant Massif after De Vos et al. (1993b) and Debacker (2012). Location of the 2008–2010 Walloon Brabant seismic swarm at Court-Saint-Etienne is indicated. The dashed line shows the trace of the Asquempont detachment fault around the Brabant Massif. b) Bouguer gravity anomaly after De Vos et al. (1993a) showing a low density Cambrian core and a high density Ordovician and Silurian rim. The 2008–2010 seismic swarm is situated at a gravity gradient marking the transition of the Cambrian core and the Ordovician and Silurian rim of the Brabant Massif. Aeromagnetic lineaments (black lines) of c) are indicated. gl: gravity low. c) The aeromagnetic map shows prominent NW–SE-oriented crustal lineaments in the Cambrian core of the Brabant Massif highlighting an arcuate shape of the slate belt. Historical seismicity (white circles) and structural grain of the Brabant Massif illustrated (black lines) on the aeromagnetic reduced-to-the-pole anomaly in the central and northern part of Belgium. The 2008–2010 Walloon Brabant seismic swarm is situated in the SE part of the slate belt. The white boxes show the locations of Figs. 3 and 13. LRE: Lower Rhine Embayment. Aeromagnetic anomaly data from Belgian Geological Survey (1994).

relocation), depth (modified by the relocation) and magnitude can be found in the online supplementary data, presented in a table and in a Google Earth KML file (respectively Appendices A and C).

The individual seismic moment  $M_0$ , i.e. the amount of energy released by each earthquake, has been calculated. The cumulative energy release of  $M_0$  is dominated by the  $M_L$  3.2 event, with more than half of the total energy released during this event. Apart from the  $M_L$  3.2 event,  $M_L > 2$  events characterise most of the remaining energy release through time. The total cumulative seismic moment, i.e.  $M_0 = 2.58 \times 10^{14}$  N m would correspond to an individual earthquake with magnitude  $M_L$  3.9 using the local empirical relationship between  $M_0$  and  $M_L$  of Reamer and Hinzen (2004) applicable for the Northern Rhine region. Given the time interval of 2 years, the Walloon Brabant swarm released its seismic energy rather slowly over a small area.

The online “Did You Feel It?” macroseismic data acquisition system of the Royal Observatory of Belgium (Lecocq et al., 2009) showed that 60 events (of 239 total for the sequence), with magnitudes between

$M_L$  0.4 and  $M_L$  3.2, were felt by the local population. The macroseismic spatial distribution of the  $M_L$  3.2 event shows that this earthquake was felt at epicentral distances larger than 75 km, from Charleroi (S of Brussels) to the north of Brussels, as far east as Liège (E of Brussels). Remarkably, sometimes very small events with a magnitude as low as  $M_L$  0.4 were also perceived by the respondents. Most of these small events were actually more often heard than felt. Given these small magnitudes, this sound perception is indicative of a local high-frequency earthquake source.

### 3.2. Magnitude–frequency distribution

The recurrence of earthquakes with various magnitudes that are generated by a fault can be described as a cumulative magnitude–frequency distribution (MFD), such as that commonly described by the Gutenberg–Richter relationship (Gutenberg and Richter, 1956):

$$\log_{10} N = a - b.M \quad (1)$$

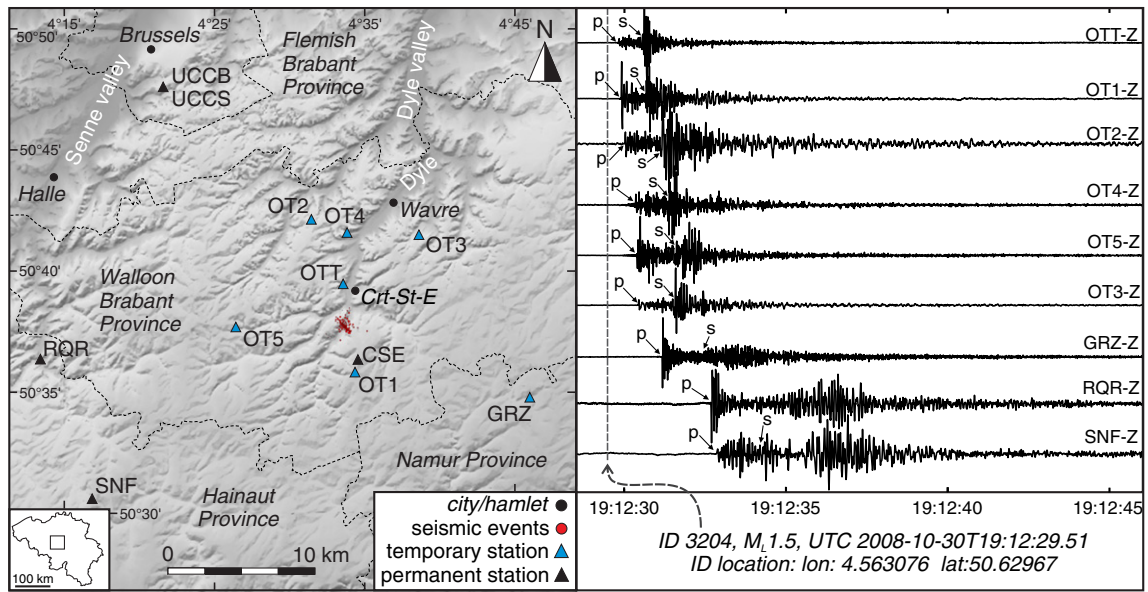


**Fig. 3.** a) Location map of the temporary seismic network (blue triangles) and the nearby permanent stations (black triangles) in the Walloon Brabant Province. Abbreviations of stations can be found in the text. The red circles show the relocated seismic events of the 2008–2010 seismic swarm. b) Waveforms of a  $M_L$  1.5 earthquake recorded by the temporary and permanent seismic networks, sorted by increasing distance to the epicentre.

where  $N$  is the number of earthquakes,  $M$  is the magnitude of those events, and  $a$  and  $b$  are the intercept and slope of a least squares best fit to the MFD, respectively. The Gutenberg–Richter relationship is effectively a measure of the relative occurrence of small to large earthquakes. The range of  $b$ -values can vary widely and depends on the nature and spatiotemporal evolution of earthquake swarms. Volcanic swarms produce  $b$ -values up to 2.5, indicating a large proportion of small earthquakes relatively to large ones, whereas  $b$ -values of non-volcanic, intraplate tectonic swarms range between 0.8 and 1.1 (Hainzl and Fischer, 2002; Ibs-von Seht et al., 2008).

The minimum magnitude of complete recording ( $M_c$ ) is an important parameter that indicates the magnitude below which no proper  $b$ -value can be calculated due to incompleteness of the dataset. This is usually expressed by a change of the slope of the MFD fit towards lower magnitudes. The MFD for the 2008–2010 seismic swarm shows that small-magnitude events between  $M_L$  0.0 and  $M_L$  0.8 are well represented (Fig. 5a). Below magnitude  $M_L$  0.4, the slope of the cumulative MFD changes considerably. This is partly because small events were not recorded before the local network was fully operational and also

because human and industrial activity during daytime hours resulted in low signal-to-noise levels. This is particularly apparent in the magnitude versus time plot (Fig. 5b). Seismic events with magnitude below  $M_L$  0.4 in the swarm catalogue could only be detected during evening- and nightly hours (18 h00–06 h00). This suggests that the catalogue is incomplete and underrepresented for events below  $M_L$  0.4. Based on the 89 events below  $M_L$  0.4 that were picked during the night (18 h00–06 h00), one may add the same number of 89 events below  $M_L$  0.4 to the 239 detected events in the catalogue to account for those events that were missed during the working hours. Such a modified catalogue of 328 events would, however, only slightly affect the  $b$ -value as only low magnitudes would be added.

For  $M_c = M_L$  0.4,  $a$ - and  $b$ -values are 2.017 and 0.662 ( $\pm 0.065$ ), respectively. The obtained  $b$ -value of the 2008–2010 catalogue is only a little lower than the 0.745 ( $\pm 0.040$ )  $b$ -value calculated for the entire instrumental catalogue (since 1983) of the Royal Observatory of Belgium (ROB) representative for the background seismicity in and around Belgium. This small difference in  $b$ -value is likely due to the differences in the study area, i.e. seismicity along one fault for the seismic

**Table 1**

Location of temporary and permanent stations and their installed equipment.  $d_{\text{epi}}$ : Epicentral distance of each station to the relocated epicentre of the  $M_L$  1.5 event shown in Fig. 3.

Station	Name	Longitude	Latitude	$d_{\text{epi}}$ (km)	Altitude (m)	Seismometer	Installation	End time
OTT	Ottignies	4.5600	50.6590	3.27	77	CMG-3ESPC	7/14/2008	8/6/2010
OT1	Mellery	4.5729	50.5971	3.69	156	LE-3D	8/11/2008	8/6/2010
OT2	Rixensart	4.5251	50.7041	8.70	102	LE-3D	8/12/2008	8/6/2010
OT3	Dion-le-Mont	4.6440	50.6934	9.09	102	LE-3D	8/12/2008	8/6/2010
OT4	Limal	4.5644	50.6948	7.24	84	LE-3D	8/11/2008	1/19/2009
OT5	Genappe	4.4409	50.6284	8.62	130	LE-3D	8/11/2008	7/20/2010
GRZ	Grand-Leez	4.7670	50.5790	15.45	152	CMG-3ESPC	7/14/2008	8/6/2010
CSE	Court-Saint-Etienne	4.5767	50.6061	2.79	157	CMG-3ESPC	Permanent since 2010-07-13	
UCCB <sup>a</sup>	Uccle	4.3605	50.7973	23.47	-10	CMG-3T	Permanent	
UCCS <sup>b</sup>	Uccle	4.3605	50.7973	23.47	104	CMG-3ESPC	Permanent	
SNF	Seneffe	4.2820	50.5077	24.05	108	L4-C	Permanent	
RQR	Ronquières	4.2246	50.6062	24.02	40	L4-C	Permanent	
SKQ	Steenkerque	4.0796	50.6487	34.16	63	LE-3D	Permanent	

<sup>a</sup> UCCB: seismometer installed in the basement rocks of the Brabant Massif in a 114 m deep borehole.

<sup>b</sup> UCCS: surface seismometer above UCCB.

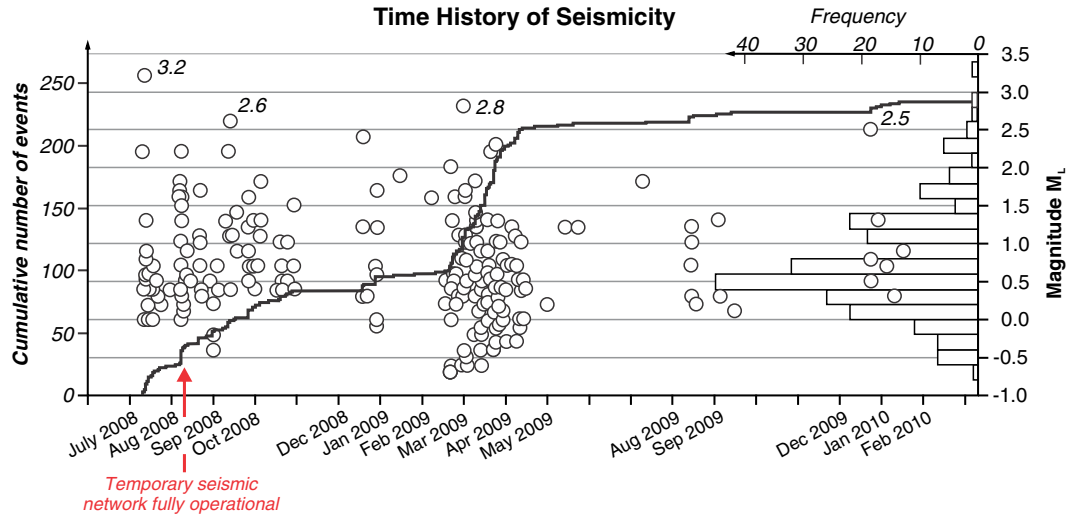


**Fig. 4.** Time history of seismicity of the 2008–2010 seismic swarm (circles), cumulative number of events (black line) and local magnitude of earthquakes (horizontal bar). The histogram displays the distribution of events in function of magnitude steps of  $M_L$  0.2. Five periods of increased seismicity are detected: summer 2008, winter 2008, spring 2009, autumn 2009 and winter 2010. There is no relationship between the temporal history of earthquake occurrence and earthquake magnitude.

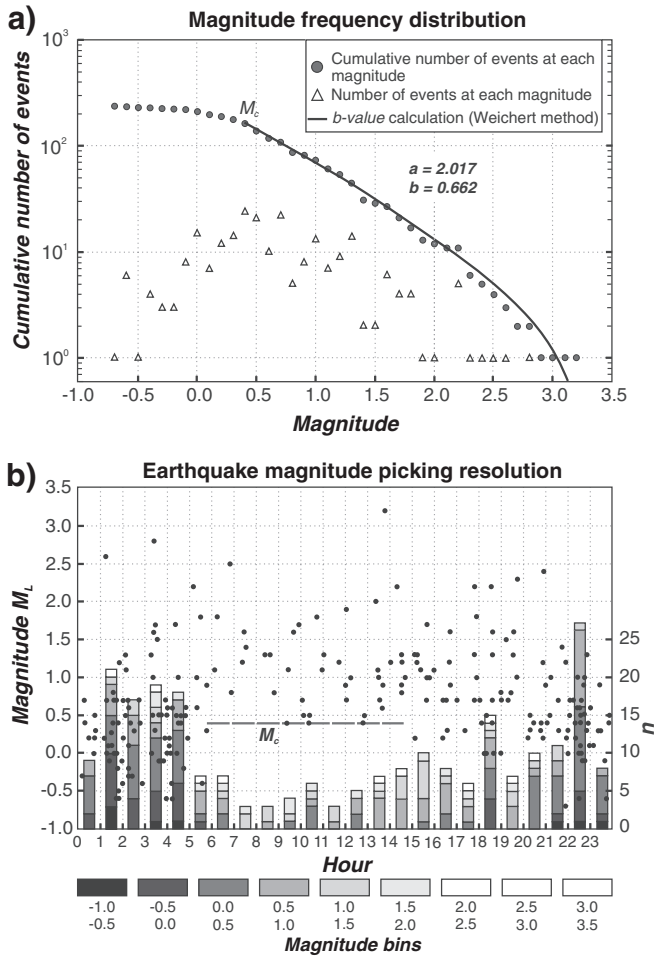


**Fig. 5.** a) Individual and cumulative magnitude frequency distribution (MFD) for the entire 2008–2014 earthquake catalogue (239 events). The  $a$ - and  $b$ -values of the Gutenberg–Richter relationship have been calculated for the range of  $M_c = 0.4 < M_L < 2.5$  and are 2.017 and 0.662, respectively. b) Resolution of the picked events after installation of the local seismic network. Due to low signal-to-noise ratio during daytime hours (6 h–18 h), the minimum magnitude of detection was  $M_L$  0.4. During the night-time hours events down to  $M_L$  -0.7 could be picked. Magnitude completeness ( $M_c$ ) of the seismic catalogue is therefore set at  $M_L$  0.4.

swarm versus background seismicity for whole Belgium, rather than to differences in catalogue length or magnitude completeness. Due to the low amount of events,  $b$ -value changes during the seismic swarm for the individual swarm periods could not be calculated. The  $b$ -value of the seismic swarm is in agreement with the low  $b$ -value of 0.8 calculated from other intraplate seismic swarms (Hainzl and Fischer, 2002; Ibs-von Seht et al., 2008). Additionally, it has to be noted that global  $b$ -values for seismic swarms in literature are sometimes calculated from moment magnitudes ( $M_w$ ), whereas the  $b$ -value of the Walloon Brabant seismic sequence is calculated from local magnitudes. Based on local conversions between  $M_L$  and  $M_w$ , the  $b$ -value estimated from  $M_L$ , however, will slightly underestimate a  $b$ -value estimated from  $M_w$ . Nevertheless, our results interestingly indicate that individual structures or an individual fault delineated by earthquake swarms can produce a robust Gutenberg–Richter relationship, something that has been questioned (e.g. Hofmann, 1996).

3.3. Earthquake location, waveform cross-correlation and event relocation

To determine the structure that was responsible for the seismic sequence, it was necessary to relocate all the determined event locations with a greater precision. For each seismic event, the P- and S-phases have been picked visually when feasible. The epicentre location of each event is computed using Hypo2000, i.e. a ROB-modified version of Hypo71 (Lee and Lahr, 1972). This modified algorithm computes 500 locations (instead of one in Hypo71) for each earthquake event by adding or subtracting non-Gaussian, random noise to P- and S-wave measurements, with a maximum error of 0.05 s and 0.10 s, respectively. The centroid of an ellipsoid containing 95% of the 500 location “cloud” is then taken as final location solution and a non-linear error in the absolute location of each epicentre is determined by evaluating the size of the cloud.

Many P- and S-events of the seismic swarm have very similar waveforms (Lecocq, 2011). As the seismic sequence seems to occur in a very small volume, relocation tools are applied in order to improve the relative location between nearby events by calculating travel time corrections between events and stations. To execute this task the double-difference algorithm HypoDD (Waldhauser and Ellsworth, 2000) is used. This software method compares travel times of closely located events recorded at a single station, allowing further improvement of the hypocentre locations (Schaff and Waldhauser, 2005). Cross-correlation differential times for HypoDD are obtained by using hypoDDpy (Krischer, 2015) and ObsPy (Beyreuther et al., 2010).

Clustering has been done using the Correlation Toolbox from the GISMO suite, a Matlab toolbox for seismology (University of Alaska Fairbanks). In the relocation method, the first P- and S-wave arrivals of each event, recorded either at a permanent or at a temporary single station, are mutually compared in a time frame window to the P-wave and S-wave arrivals of all other events recorded at the same station (Fig. 6). Waveform similarity of co-located earthquakes indicates that the source of these events is nearly equivalent and that the ray trajectories from source to receiver are at about the same and travelled through an almost identical medium. Differences between travel times are then solely attributed to the corresponding distance between hypocentres. Identification of repeated events or multiplets can be performed either by comparing all traces visually or by calculating the cross-correlation coefficient of an event that is cross-correlated with all other events in a similarity cross-correlation matrix, indicating the degree of waveform similarity between events (e.g. Barani et al., 2014). The correlation function only measures the normalised similarity of the waveform shape but not the amplitude of the events. For events with a higher correlation the travel path will be identical but the strength of the source might differ.

For the measurements of the differential times, a window length of 0.25 s, i.e. 0.05 s before and 0.20 s after pick time, was used. Waveforms were bandpass filtered between 1 and 20 Hz. The minimum correlation coefficient similarity threshold allowed is 0.75, meaning that 75% of waveform similarity had to be fulfilled before they could be used in the double-difference procedure. Cross-correlation shows that many of the events of different swarm activity periods show similar waveforms. For the Spring 2009 activity, for example, cross-correlation shows that 49 events of all 239 events recorded at the Ottignies station (OTT, station deployed directly on the basement rocks of the Brabant Massif) show a waveform similarity of more than 75% (Fig. 6a, b). Events of the Autumn 2008 period also show a high similarity (Fig. 6c, d). Cross-correlation thus demonstrates the tight spatial grouping of the events.

In the original locations of the seismic swarm (white dots in Fig. 7), most events cluster in a dense cloud from which the first two  $M_L$  2.2 and  $M_L$  3.2 earthquakes are separated by a northward offset of 900 m (see locations of  $M_L$  2.2 and  $M_L$  3.2 in Fig. 7). This offset is attributed to the absence of the local network during the two first events. In order to calculate the precise focal mechanisms of these two large

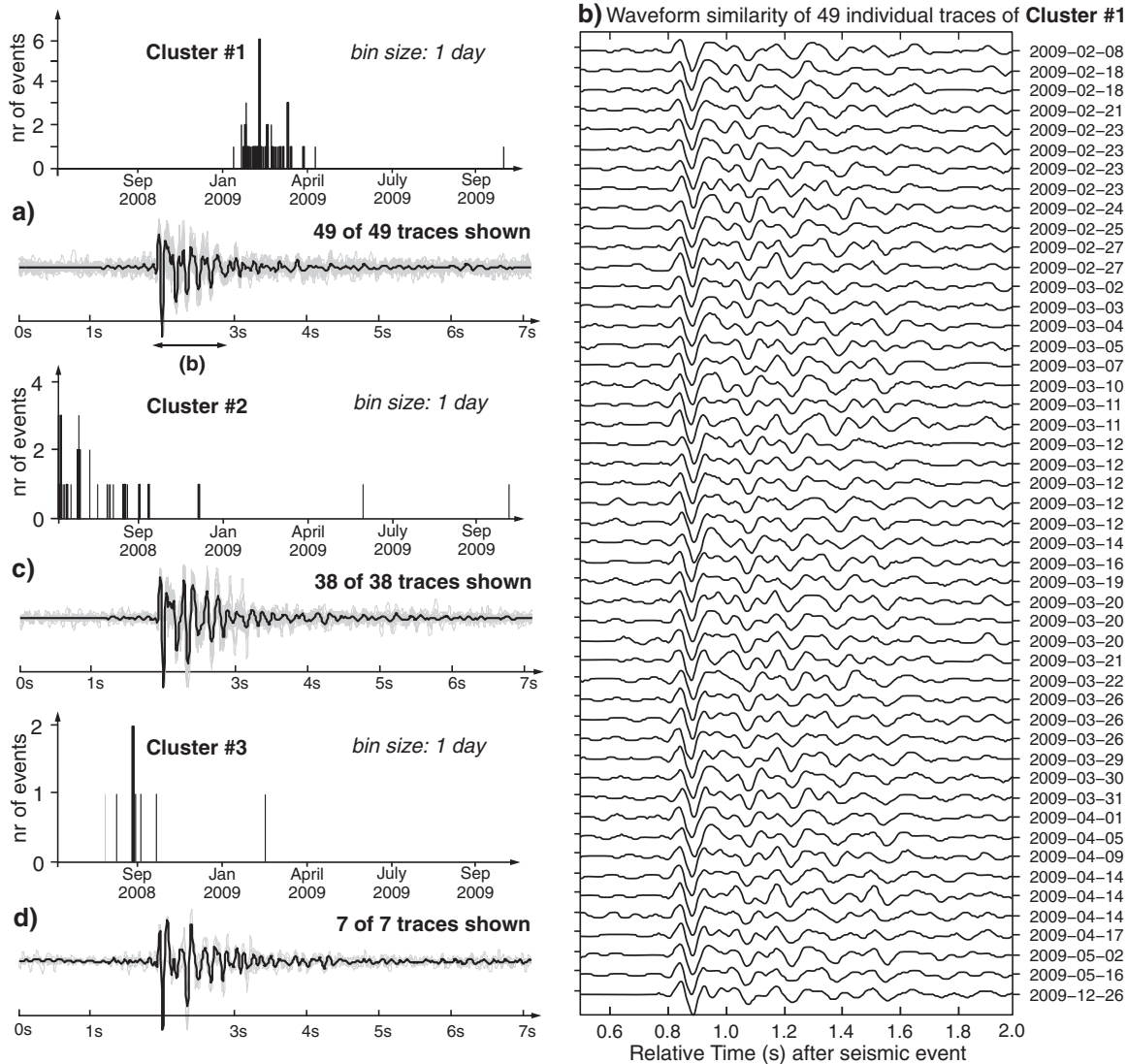


**Fig. 6.** Example of waveform comparison, event clustering and overlay of events recorded at the Ottignies (OTT) temporary seismic station. All first P-wave arrivals of different events are aligned in order to correlate and compare the different waveforms. This allows refinement of the arrival times and the hypocentre locations. Three different clusters can be deduced. a) Cross-correlation of waveforms of the Spring 2009 activity shows a high similarity. b) Cross-correlation of 49 individual traces. Note that the first 0.6 s after the first P-wave arrival is strikingly similar for all events. c) Cross-correlation shows that 34 events of the Autumn 2008 activity are comparable to 4 other events of the swarm. d) Cross-correlation and timing of additional 7 events.

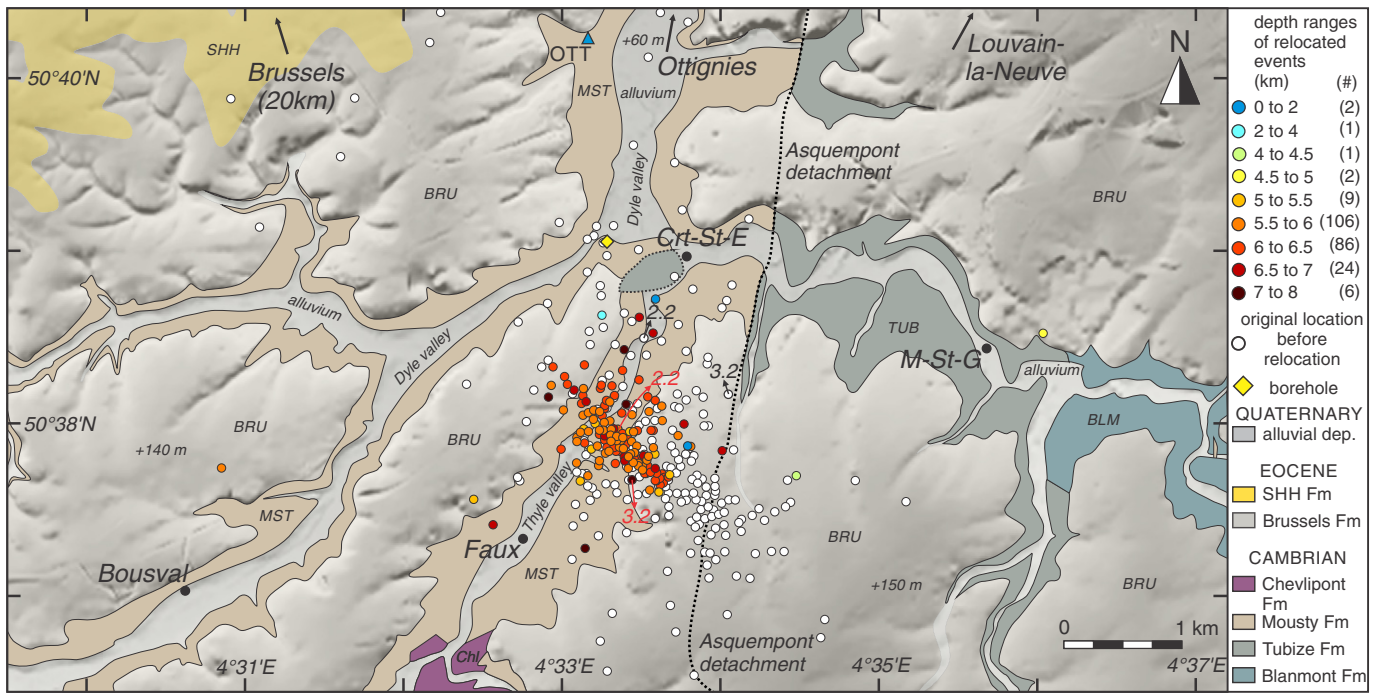


**Fig. 7.** Simplified geological map of epicentral area. The Thyle and Dyle river valleys have incised into the Cambrian basement rocks of the Brabant Massif. These rocks are covered by sandy Eocene formations (BRU, SHH) on hill tops. The epicentral distribution of the seismic swarm before (white dots) and after (dots coloured by depth) relocation by cross-correlation is shown. The original (in black) and relocated (in red) locations of the first two events, i.e. the  $M_L$  2.2 and  $M_L$  3.2, are indicated. The relocated epicentres delimit a narrow NW–SE oriented fault dipping steeply to the NE. The contact between the Tubize (TUB) and Mousty (MST) Formation indicates the position of the Asquemont detachment fault (dotted grey line). Basemap is the digital elevation model (©Nationaal Geografisch Instituut) of the epicentral area. Crt-St-E: Court-Saint-Etienne; M-St-G: Mont-Saint-Guibert; OTT: temporary station Ottignies. SHH: Sint-Huibrechts-Hern.

events (see section 3.5), these two events needed to be relocated properly. Based on the strongly comparable waveforms and on the large cross-correlation in the similarity matrix of the Steenkerque seismic station (SKQ in Table 1 and Fig. 3), the July 12 2008  $M_L$  2.2 and July 13 2008  $M_L$  3.2 events cross-correlate to the waveform of the September 13 2008  $M_L$  2.6 event and to other minor events in the September cluster. The waveforms of the September 2008 cluster on their turn cross-correlate to many of the events of the Spring 2009 cluster. Consequently, given the large similarity of these different events, the  $M_L$  2.2 and  $M_L$  3.2 events can be relocated relatively close to the other clusters (see relocated position of  $M_L$  2.2 and  $M_L$  3.2 in Fig. 7). Cross-correlation thus corrects for the northwards shift of the epicentre location of the first two large earthquakes in the final seismic swarm earthquake catalogue (see Appendix A). This northward error is no longer present for all subsequent events because of the installation of the temporary network, with the closest Ottignies station (OTT) at 2.5 km and 3.5 km from the NW and SE end of the seismic swarm, respectively. All events that took place after the local network was removed, e.g. such as the 14 January 2014 event (see Appendix A), are still cross-correlated with the 2008–2010 events to relocate these new events.

By cross-correlation, the manually picked P- and S-wave arrival times could be refined to subsample spacing of a few milliseconds (below 0.008 s for 125 Hz sampling rate, Deichmann and Garcia-Fernandez, 1992). Afterwards, these new picks are used as an input to HypoDD to improve the quality of the original hypocentre locations.

By considering the difference in travel times between the different events, the original location of the Walloon Brabant seismic swarm was considerably improved. The relocated hypocentres form a dense cluster both in horizontal and vertical direction (Figs. 7 and 8). The double-difference locations strongly improved the precision of the relative positions of the individual events, with a very small error of 10 m on the relative locations. Ultimately, the orientation of the relocated epicentres suggest that the swarm occurred along a narrow,

1.5 km-long NW–SE oriented fault structure north of Faux, a small hamlet in the Thyle valley 3 km south of Court-Saint-Etienne (Fig. 7). The relocated dataset is available in the Online Supplementary as a dataset (Appendix A) and as a Google Earth KML-file (Appendix C). An uncertainty in the accuracy of the absolute position of the entire seismic swarm needs to be considered. Although picking errors, site- and path effects are removed after relocation, local site effects (at places where the temporary station are deployed) and path effects (affecting the local crustal velocity) can influence the absolute location of the swarm. Errors indicate that the absolute location can move 0.5 km north- or southwards. However, based on detailed macroseismic answers of people responding to the sound produced by very low-magnitude earthquakes of the seismic swarm (e.g. 12 responses to a  $M_L$  0.7 event), the determined absolute location is quite accurate as people regularly reported the area north of Faux in the Thyle valley (Fig. 7) as the exact sound source of the event.

Relocating all hypocentres allows performing a 3D analysis on the relocated hypocentre distribution in function of depth versus time of occurrence (Fig. 8a). From this hypocentre distribution it is clear that the swarm activity is restricted to a rather narrow volume situated between 5 km and 7 km depth, with exception of the  $M_L$  3.2 event that has been relocated to a depth of 7.74 km, although it has to be noted that this event has a larger uncertainty in depth estimation due to relocation. The error in depth estimation is quite low as the temporary stations are deployed at maximum half of the epicentral distance.

To estimate the true dip of the fault structure, we use the method of Camelbeeck (1993), which describes an ellipsoid defined by 95% of the hypocentres. Applying this method to the hypocentre cloud of relocated events shows that the NW–SE fault structure dips steeply to the NE at an angle of  $\sim 87^\circ$  (Fig. 8a). The swarm is thus clearly limited both in vertical and horizontal dimension.

Only in very short time slots, a spatial distribution and depth correlation can be found. For example, 6 events of the Spring 2009 cluster occurred within three hours (i.e. between 2009-03-26-

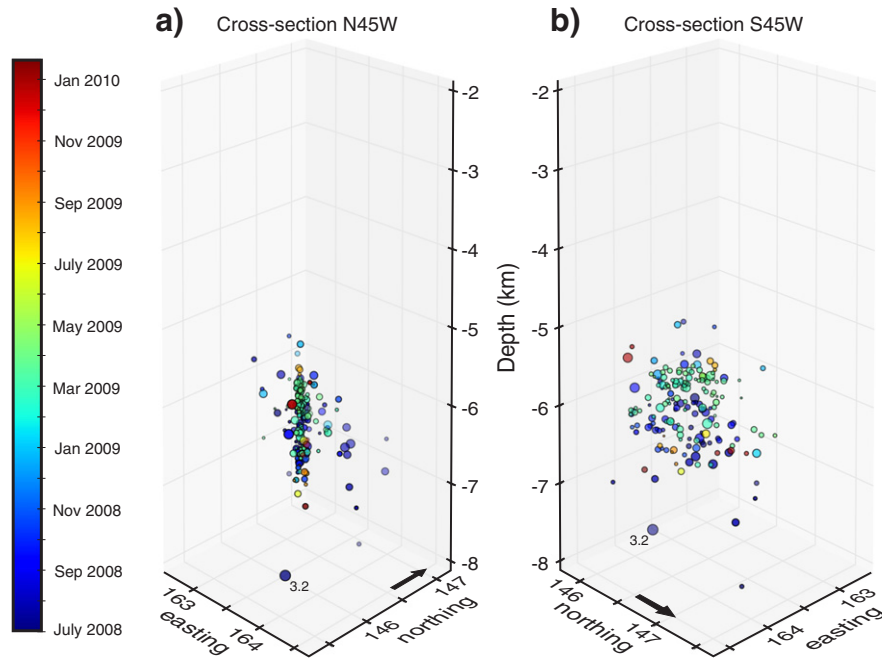


**Fig. 8.** Three-dimensional relocated hypocentral distribution of the 2008–2010 seismic swarm (circles) as a function of depth and time past after the first event. The colours display the temporal evolution of the earthquake swarm from the first event (12-07-2008) onwards. Note the linearity of the events and the limited horizontal distribution of the swarm. The size of the circles corresponds to the magnitude variation within the swarm. The  $M_L$  3.2 event is indicated. a) N45W cross-section parallel to the fault structure. b) S45E in plane section perpendicular to the fault. The horizontal axis is in local Belgium Lambert 1972 coordinates (kilometre scale); vertical and horizontal dimensions are to scale. Black arrow denotes North.

22:31:19 and 2009-03-27-01:57:12). Spatially, these events were only separated from each other by a distance of 100 m (between 5.846 km and 5.947 km depth; see event numbers 180–185 in the catalogue in the supplementary data). Similarly, other depth correlations can be found in other very short time windows. However, if the whole swarm is considered, little, if any, correlation between depth and rupture propagation through time can be found. This absence of correlation conflicts with fluid- or gas-driven seismic swarms that are characterised by an upward migration of events.

### 3.4. Fault plane solutions

The focal mechanism is the geometric description of the brittle deformation produced by earthquakes. These were calculated from the P-wave first motion polarities of the individual earthquakes that arrive at different seismic stations using *fpsol*, an algorithm that computes the nodal planes by a grid search on the possible strike, dip and slip minimising the misfit between theoretical and observed P-wave first motions projected on the focal sphere (Camelbeek, 1993). The calculation of focal mechanisms allows determining the orientation (strike, dip) and slip vector on each plane of the fault structure. These can then be used to derive the associated tectonic stress responsible of the fault and thus of the earthquake activity. The Belgian network geometry and station spacing allowed for the determination of 10 fault plane solutions for events  $> M_L$  1.6 with a small 95% confidence region on the focal sphere indicating good solutions. For each of these fault plane solutions, the focal sphere was centred on the relocated hypocentre, assuming that the relocations provide a better homogeneity of the dataset (Fig. 9). Using the original locations instead of the relocated locations, however, did not significantly change the obtained focal mechanisms as the most important factor is the depth estimation.

The comparison between the spatial distribution of relocated earthquakes (Fig. 7) and their focal mechanisms show a clear match between one of the two nodal planes and the distribution. Based on the spatial distribution of the different events, the distinct, steeply dipping, NW–SE fault structure automatically distinguishes the NW–SE nodal planes

as the actual fault plane and the NE–SW-oriented planes as the auxiliary planes (Table 2, Fig. 10). The focal mechanisms indicate left-lateral oblique to purely left-lateral strike-slip movement of the nearly vertical fault as the driving force of the seismic swarm.

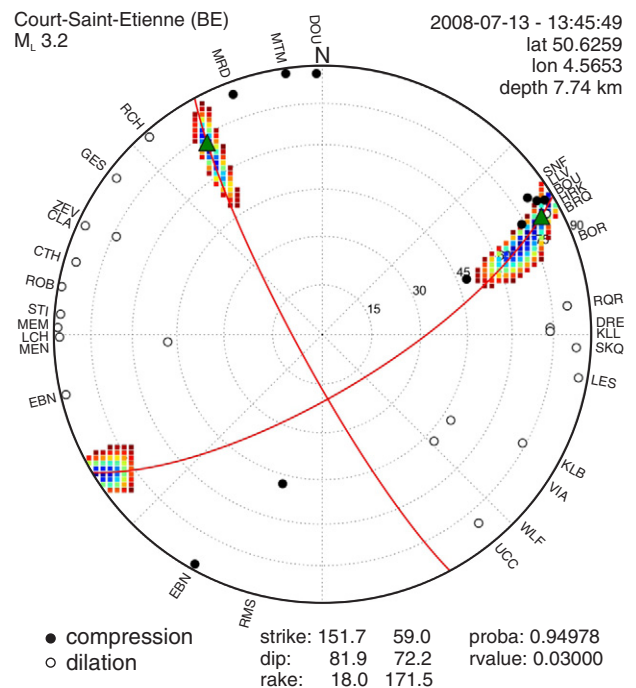


**Fig. 9.** Focal mechanism computation of the  $M_L$  3.2 event (at a depth of 7.74 km) on the focal sphere. Degrees in the focal sphere correspond to the angle of the position of the seismic station relative to the event. The coloured contours represent a 95% probability. Explanation of the station abbreviations of the Belgian network can be found on [www.seismology.be](http://www.seismology.be). UCC = Uccle station.

**Table 2**

Database of the 10 reliable earthquake focal mechanisms of the 2008–2010 seismic swarm used for stress inversion. Location gives the orientation after relocation.  $M_L$  = local earthquake magnitude. Strike, dip and rake of the nodal plane interpreted as the fault plane and the auxiliary nodal planes are given. SH: horizontal shortening.

Event		Location			Magn.	Fault plane			Nodal plane			SH		Stress
ROB-ID	Time	Lon	Lat	Depth	$M_L$	Strike	Dip	Rake	Strike	Dip	Rake	Max	Min	Regime
3069	20080713-13:45:49	50.62587	4.565332	7.740	3.2	151.7	81.9	18.0	59.0	72.2	171.5	105	15	SS
3090	20080808-09:54:39	50.63412	4.564285	6.336	1.7	119.2	74.0	0.9	28.9	89.1	164.0	74	164	SS
3094	20080808-17:52:02	50.62817	4.560497	5.474	1.8	133.0	73.7	-62.0	250.8	32.1	-148.1	102	12	NF
3165	20080912-05:08:55	50.62995	4.562925	6.406	2.2	341.8	72.0	32.0	240.8	59.7	159.0	111	21	SS
3225	20081220-20:53:08	50.62695	4.566024	5.652	2.4	318.8	80.1	-30.0	54.4	60.5	-168.6	97	7	SS
3232	20081229-03:27:55	50.62709	4.558643	5.715	1.7	123.0	70.4	-12.5	217.2	78.3	-160.0	80	170	SS
3239	20090115-12:02:24	50.63454	4.559644	6.458	1.9	139.5	72.0	-20.0	235.9	71.0	-160.9	98	8	SS
3273	20090303-03:23:32	50.62994	4.561393	6.264	2.8	319.8	82.2	-20.0	52.6	70.2	-171.7	96	6	SS
3276	20090305-04:21:42	50.62936	4.561387	6.088	1.7	310.7	49.7	-35.0	65.1	64.0	-134.0	98	8	NS
3552	20091226-06:50:13	50.62489	4.568443	5.469	2.5	324.7	82.8	-6.0	55.5	84.0	-172.7	101	11	SS

Stress regime: SS = strike-slip; NF = formal faulting; NS = combined normal and strike-slip faulting.

3.5. Stress inversion

Principal stress orientations active during faulting can be derived from fault slip data along representative faults. Stress inversion assumes the Wallace–Bott hypothesis (Bott, 1959; Wallace, 1951), which states that slip occurs parallel to the resolved shear stress on a pre-existing or along a newly formed fault plane. The inversion technique involves the concept of (i) deriving the best-fitting stress tensor capable of explaining the direction of slip along the fault and (ii) deriving the magnitude of the principal stress directions. In this method, the data are first processed interactively using the Right Dihedral Method (Angelier and Mechler, 1977) optimised in the Win-Tensor programme (version 4.0.4), a software tool specifically developed for the derivation of the orientation of the principal stress axes of the regional stress tensor (Delvaux and Sperner, 2003). The Right Dihedral Method is independent of the choice of nodal planes and gives a range of possible orientations of  $\sigma_1$ ,  $\sigma_2$  and  $\sigma_3$ . The iterative grid search “Rotational Optimisation” method is applied to the results of the inversion by using a misfit (F5 in the Win-Tensor programme, see Delvaux and Sperner, 2003 for details).

By using the Win-Tensor programme, first both nodal planes of each calculated focal mechanism, with their accompanying slip lines, are inverted to a stress tensor. As the alignment of hypocentres identifies the NW–SE oriented nodal plane in the focal mechanism as the true fault plane and the NE–SW oriented planes as the auxiliary plane, the final inversion includes only those focal planes that best fit to the local stress field. The graphical output of the inversion into an equal-area stereographic projection then allows evaluation of the overall quality of the stress inversion. During the inversion process, an exponential weighting factor that is a function of the magnitude of the earthquakes is used. This factor effectively emphasises higher magnitude events.

Stress inversion of the 10 different focal mechanisms shows a local WNW–ESE oriented  $\sigma_H$  ( $\sigma_1 \sim 08/095$ ), NNE–SSW  $\sigma_h$  ( $\sigma_3 \sim 12/187$ ) and a nearly vertical  $\sigma_v$  ( $\sigma_2 \sim 76/331$ ) which correspond to a left-lateral and nearly pure strike-slip stress regime with maximum horizontal stress ( $\sigma_H$ ) oriented N275° (Fig. 11). The orientation of individual stress axes are indicated in a plunge/trend convention. The relative magnitude of the three principal stresses, i.e. the stress ratio  $R = (\sigma_1 - \sigma_2) / (\sigma_1 - \sigma_3)$ , has a value of 0.46 and defines three different stress magnitudes indicative of the pure strike-slip nature of the

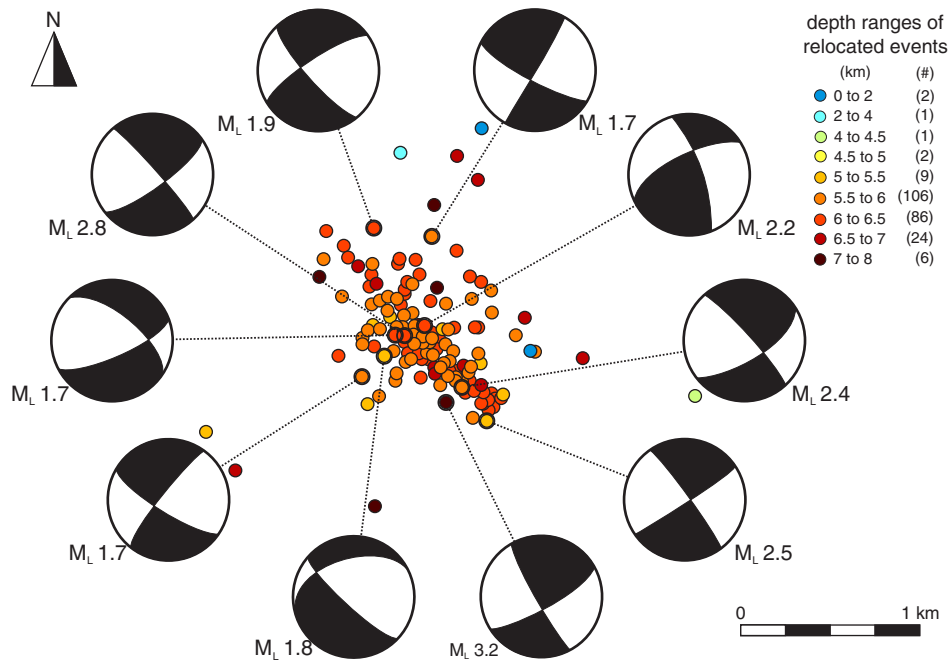


**Fig. 10.** Focal mechanisms of all events for which a reliable mechanism could be calculated. The seismic swarm is dominated by left-lateral strike-slip motion. The orientation of the swarm indicates that the NW–SE nodal planes can be interpreted as the true fault plane. See Table 2 for the details of the focal mechanisms.

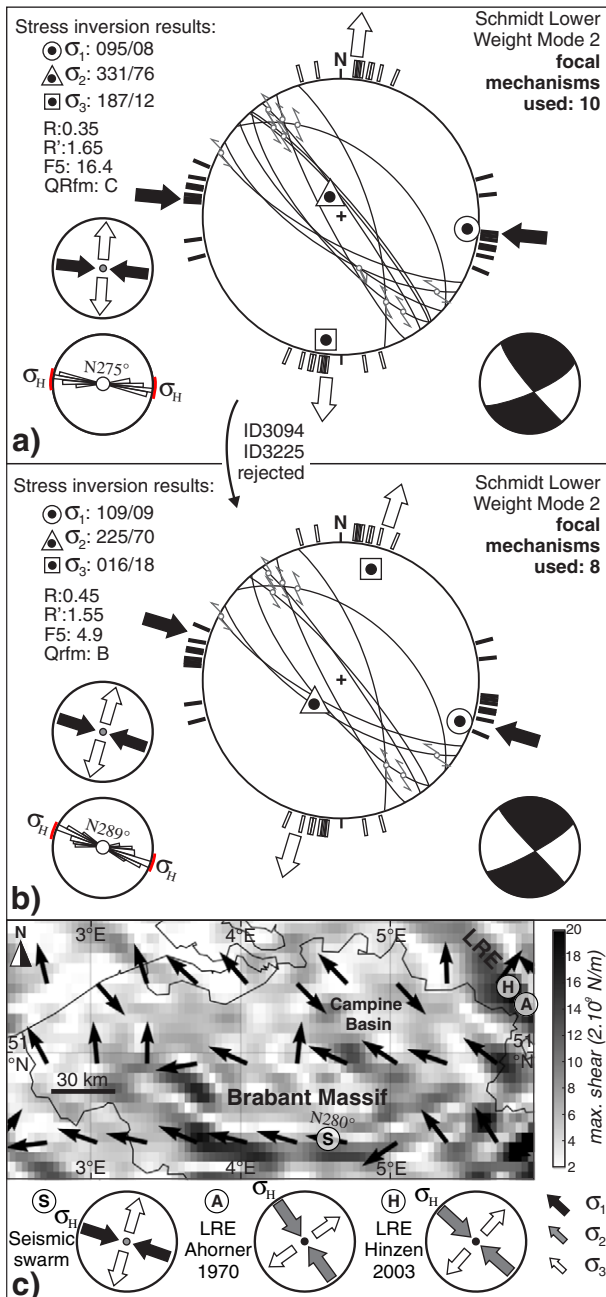


**Fig. 11.** Lower-hemisphere equal-area stereoplots of the true nodal planes showing stress inversion results (Win-Tensor programme). Results are represented by (i) the orientation (in plunge/trend convention) of three principal stress axes and (ii) the direction of  $S_{Hmax}$  (black arrows) and  $S_{Hmin}$  (white arrows). The bars outside the stereograms show the stress inversion result of each individual focal mechanism ( $\sigma_H = \text{black}$  and  $\sigma_h = \text{white}$ ). The lower right inset shows the corresponding focal mechanism of all weighted fault plane solutions. The two lower left insets show the maximum principal component ( $\sigma_H$ ). The uncertainty of  $\sigma_H$  is expressed by the red bars outside the lower left stereoplot and is within the range of the individual stress inversion bars. a) Inversion of 10 selected events representative for the seismic swarm.  $\sigma_H$  has a  $N275^\circ$  (WNW–ESE) orientation but a high misfit of 16.4%. b) Rejection of a normal and oblique event results in a lower misfit (4.9%) and a more reliable stress tensor with a  $\sigma_H$  oriented  $N289^\circ$  (WNW–ESE). R = stress ratio; QRfm = quality factor of stress tensor following World Stress Map criteria (C = medium, B = good); F5 = misfit function of results (Delvaux and Sperner, 2003); R' = stress regime index ( $R' = 2 - R$  for a strike-slip regime). c) Map showing local stress variation in central and north Belgium estimated from differences in the gravitational potential energy after the method of Camelbeeck et al. (2013). Black arrows indicate local stress orientations. LRE: Lower Rhine Embayment. S = location of the seismic swarm. Note the similarity between local stresses and the stress orientation derived in b).

seismicity (Table 3). It has to be noted that there is an uncertainty in the stress tensor as only 10 focal mechanisms of the swarm are analysed. The uncertainty (expressed as the misfit function F5 in Fig. 11; Table 3) is improved considerably after removal of a normal (ID 3094) and an oblique (ID 3225) event, resulting in a slightly different stress tensor with an orientation of  $N289^\circ$  for  $\sigma_H$ .

#### 4. Comparison of the 2008–2010 and 1953–1957 seismic sequences

An earlier seismic sequence took place a few kilometres south of Court-Saint-Etienne between 1953 and 1957. Only the largest events of this sequence were recorded by the Uccle seismic station, which was the only operational seismic station in Belgium in 1953. At that time, one vertical (1300 kg) and two horizontal (1000 kg) Wiechert seismographs were installed in the Uccle seismological lab. Vertical, E–W and N–S horizontal ground motions were recorded by printing earthquake waveform data on smoked paper (Charlier and Van Gils, 1953).

The 1953–1957 seismic sequence started on 5 January 1953 with a  $M_L$  4.0 earthquake and was followed by two  $M_L$  3.6 and 3.4  $M_L$  events on 28 August 1953 (data from the ROB catalogue, [www.seismology.be](http://www.seismology.be)). Three years later, on 21 April 1956, a  $M_L < 3.0$  occurred. However, historical records from testimonies of people living in the epicentral area at Court-Saint-Etienne report that four different events were felt on 5 January 1953, although only one event was recorded at Uccle. It is thus possible that the 1953–1957 sequence might also have been a seismic swarm of which the spatiotemporal evolution is unfortunately unknown due to the absence of recordings of the small-magnitude events.

A comparison between the Z-component waveforms of the 5 January 1953 event recorded using the historical Wiechert seismograph and those of the largest events of the 2008–2010 swarms recorded by the Guralp broadband seismometer (CMG-3ESPC) located next to the Wiechert seismograph at Uccle shows notable similarity (Fig. 12). We used a classical restitution filter of the displacement (Scherbaum, 2001) of the Guralp recordings in order to compare waveforms of different instruments. The time period range between the P- and S-wave arrivals of the five largest earthquakes of the 2008–2010 sequences is between 2.38 s and 2.82 s (Table 3). The time period for the 5 January 1953 event is between 2.3 s and 2.8 s, indicating that travel distance from the source of the different earthquake events to the seismometer at Uccle was almost similar for the 1953 event and the largest of the 2008–2010 events. It is worth noting the S-wave asymmetry for both sequences: it shows first a minor negative amplitude ( $\sim -33.5 \mu\text{m}$  and  $-8.1 \mu\text{m}$  for  $M_L$  4.0 1953 and  $M_L$  3.2 2008, respectively) and then a large positive amplitude ( $\sim 55 \mu\text{m}$  and  $14.7 \mu\text{m}$  for  $M_L$  4.0 1953 and  $M_L$  3.2 2008, respectively; Table 4; Fig. 12). Also the peaks following the first S-wave arrivals all have a similar waveform pattern. This indicates an identical travel path of earthquake waves from the source to Uccle. The maximum S-wave amplitude of the 1953  $M_L$  4.0 earthquake is at least four times as large as the maximum S-wave amplitude of the 2008  $M_L$  3.2 earthquake. Considering these similar amplitude changes, the source and focal mechanisms of the 2008–2010 and 1953 earthquakes are likely similar.

Due to a lack of recorded data and the absence of a dense seismometer network in the 1950s, the different events of the 1953–1957 earthquake sequence cannot be re-located properly. However, a rough event location with an error of 5 km could be derived from the macroseismic distribution of felt events. The epicentre location of the 1953 and 1957 events were estimated to lie in the vicinity of the Héவில்lers hamlet, 4 km SE of the epicentral area of the 2008–2010 swarm. However, given the large error in earthquake location based on macroseismic data and on the similarity in the waveforms, the 1953–1957 epicentral area might be as well be easily located in the epicentral area of the 2008–2010 swarm, suggesting that both seismic sequences may indeed have a similar source.

**Table 3**

Phase arrival time measurements at the Uccle seismic station (UCCS) of the largest events of the 2008–2010 Walloon Brabant seismic swarm and phase arrival time of the  $M_L$  4.0 1953 seismic event estimated from the scanned 1953 waveform. The timing of three other events of the 1953–1957 seismic sequence is given.

ID	$M_L$	Date	Time	P-wave arrival	Time between P- and S-wave	Zero-to-peak S-wave amplitude (nm)	P-wave polarity	Longitude	Latitude	Depth			
Nr	ROB-ID	Year	Month	Day	(h:min:s)	(h:min:s)		(°N)	(°E)	(km)			
3	3069	3.2	2008	7	13	13:45:49.96	13:45:54.40	2.38 s	14,781	Dilatation	50.6259	4.5653	7.740
56	3167	2.6	2008	9	13	01:14:17.28	01:14:20.71	2.82 s	4897	Dilatation	50.6251	4.5674	5.874
87	3225	2.4	2008	12	20	20:53:08.52	20:53:11.90	2.48 s	2140	Compression	50.6269	4.5660	5.652
118	3273	2.8	2009	3	3	03:23:32.64	03:23:36.98	2.54 s	6056	Compression	50.6299	4.5614	6.264
229	3552	2.5	2009	12	26	06:50:13.47	06:50:17.88	2.71 s	3700	Compression	50.6249	4.5684	5.469
Wie-V <sup>a</sup>	4	1953	1	6	23:58:44	–	–	2.4–2.6 s <sup>b</sup>	55,000 <sup>b</sup>	Dilatation	50.617	4.600	–
Wie-V <sup>a</sup>	3.6	1953	8	28	0:05:21								
Wie-V <sup>a</sup>	3.4	1953	8	28	0:06:16								
Wie-V <sup>a</sup>	<3	1956	4	51	22:47:07								

<sup>a</sup> Wie-V: vertical Wiechert seismogram.  
<sup>b</sup> Graphically estimated.

**5. Seismotectonic significance by matched bandpass filtering**

*5.1. Aeromagnetic interpretation of the Brabant Massif*

The tectonic grain of the buried Brabant Massif has been previously interpreted using Bouguer gravity and aeromagnetic anomaly maps and their derivatives (Debacker, 2012; Everaerts et al., 1996; Sintubin, 1997; Sintubin and Everaerts, 2002). The airborne magnetic data over the Cambrian core of the Brabant Massif were collected in 1994 with a flight line spacing of 0.5 km at a nominal height of 120 m above the ground (Belgian Geological Survey, 1994). Tie lines were 10 km apart. This flight line spacing should provide the resolution necessary for a detailed study of the seismic swarm. The raw flight lines are available in the online supplementary data (Appendix B) for an evaluation of the analysis presented in this work. Other parts of the Brabant Massif

and Belgium were covered with flight line spacing of 1.0 km. For further analyses of magnetic data, we consider the reduced-to-pole (RTP) magnetic field. Reduction to the pole is a transformation that generally aligns magnetic anomalies over the sources that generate them by showing how the magnetic field might appear if the ambient field and remanent magnetisation sources were vertical. We note that the RTP field is similar to that of the total-field anomaly, not surprisingly given the relatively steep inclination of the magnetic field (66°) in our study area.

Within the core of the Brabant Massif, the amplitude of the magnetic anomaly is primarily lithology dependant. The slaty metasedimentary rocks within the Tubize Formation (Fig. 7) of the lower Cambrian Tubize Group (Herbosch and Verniers, 2013) are considered highly magnetised and coincide with magnetic highs. Other studies in the Tubize Formation have confirmed the relationship of magnetic highs with bedding

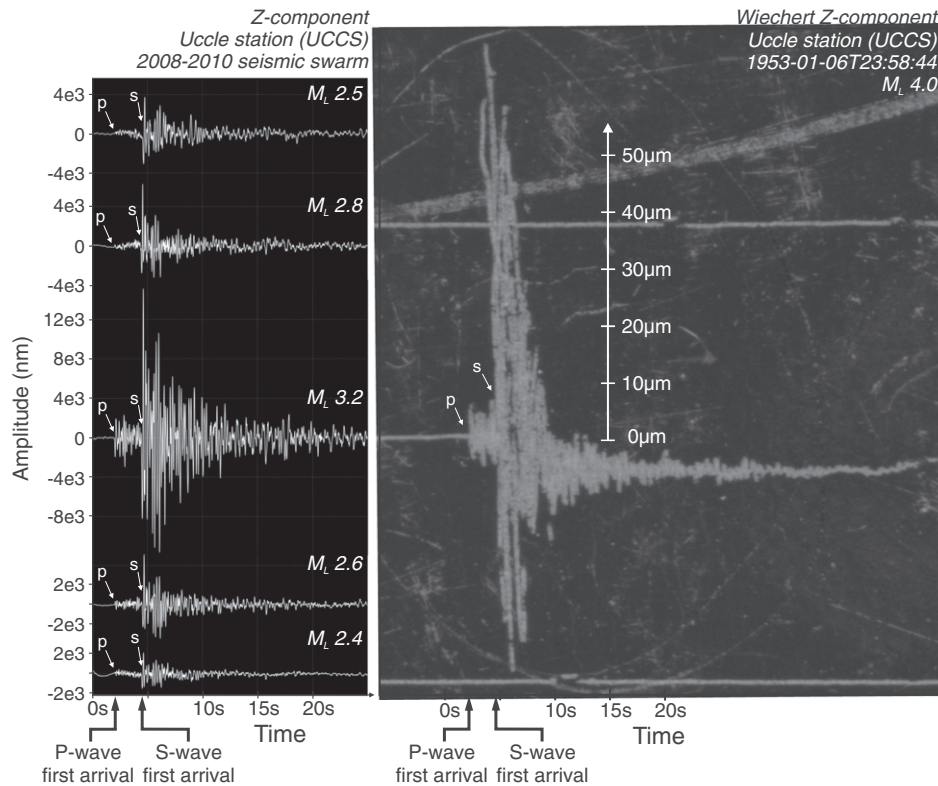


**Fig. 12.** Comparison between waveforms of the 2008–2010 seismic swarm and the 5 January 1953 event of the 1953–1957 seismic swarm. Note the waveform similarity between the Z-component of the five largest events of the 2008–2010 seismic swarm (left) and the Z-component of the 1953  $M_L$  4.0 earthquake (right). 2008–2010 waveforms are displacement restitution and highpass (0.3 Hz, 2 corners) filtered. Scan of the smoked paper of the 1953 earthquake was printed by the vertical Wiechert seismograph at the Royal Observatory of Belgium at Uccle. Note the permanent displacement of the vertical Wiechert seismograph because of the 1953 earthquake.

**Table 4**  
Bandpass filter parameters and matched-filter depths. P1–P4 represent layers. P0 represents a half-space. To estimate the real depths, the flight height of 120 m was subtracted from the filtered depths.

Filter 1				Filter 2			
Layer	Depth (m)	Real depth (m)	Amplitude	Layer	Depth (m)	Real depth (m)	Amplitude
P4	45.15	No maps shown for these depths due to flight noise	1.40E–02	P4	45.58	No maps shown for these depths due to flight noise	1.63E–02
P3	190.02		2.015	P3	202.63		2.867
P2	468.31		74.67	P2	553.34		153.7
P1	1180.73	1.1 km	886.8	P1	2144.92	2.0 km	4967
P0	4550.52	4.4 km	23.09	P0	7267.36	7.1 km	37.68

(e.g. de Magnée and Raynaud, 1944; De Vos et al., 1992; Debacker et al., 2004a; Everaerts, 2000; Vander Auwera and André, 1985).

The two NW–SE magnetic highs north of the epicentral area, i.e. at Ottignies and at Limal (Fig. 13), correspond to subsurface shallowing of the highly magnetised part of the Lower Cambrian Tubize Formation. The magnetic lows between the highs might represent the more poorly magnetised sedimentary layers within the Tubize Formation and poorly magnetised overlying formations (Debacker, 2012; Debacker et al., 2010). Various lineaments are associated with changes of large-scale fold limbs and to high-strain deformation zones that modify this formation at depth (Debacker, 2012; Everaerts et al., 1996; Sintubin and Everaerts, 2002). The most prominent of aeromagnetic lineaments is situated along the SW boundary of the Brabant Massif where they appear as step-like lineaments interpreted as dextral transpressional shear zones (Figs. 2 and 13).

Locally at Court-Saint-Etienne, a positive anomaly corresponds to surface exposures (see grey isolated lens of the Tubize Formation south of the city of Court-Saint-Etienne in Fig. 13) and shallowing of the Tubize Formation. In this area, the weakly-magnetic Upper Cambrian slaty metasediments of the Mousty Formation are mapped near the surface in the Dyle and Thyle valleys (see Fig. 7) (Delcambre and Pingot, 2002; Herbosch and Verniers, 2013). The presence of the 5-km long ENE–WSW magnetic high below Court-Saint-Etienne, however,

suggests that the Tubize Formation is still present at shallow depth below the mapped Mousty Formation at the surface (Debacker et al., 2004a). A shallow 45° S-plunging cored borehole (161 m; Herbosch, Pingot and Delcambre, unpublished data; see yellow diamond in Fig. 13) only demonstrated the presence of Mousty slates but, more importantly, showed that bedding is steeply dipping (70°–85°) to the NE near the isolated lens of the Tubize Formation.

Northwest of Court-Saint-Etienne, a NW–SE oriented, triangular-shaped aeromagnetic low (Fig. 13) coincides with the Mousty Formation on the geological subcrop map. This aeromagnetic low reflects a thick sequence of Mousty slates in a synclinal structure, strongly reducing the aeromagnetic signal of the underlying Tubize Formation (Debacker et al., 2004a; Sintubin, 1997; Van Tassel, 1986). The northern part of this triangular aeromagnetic low is bounded by a steep, N60W-trending aeromagnetic gradient separating the Mousty Formation from the Tubize Formation. Throughout the eastern part of the Brabant Massif, the contact between the Upper Cambrian Mousty and the Lower Cambrian Tubize Formation is characterised by a pre-folding, pre-cleavage low-angle extensional detachment reflecting an ~25 Ma hiatus, referred to as the Asquempont detachment (Debacker et al., 2003; Debacker et al., 2004b). This detachment is folded and can be traced following the curvature of the core of the massif (Fig. 2a). In the area around the seismic swarm, the Asquempont detachment, and

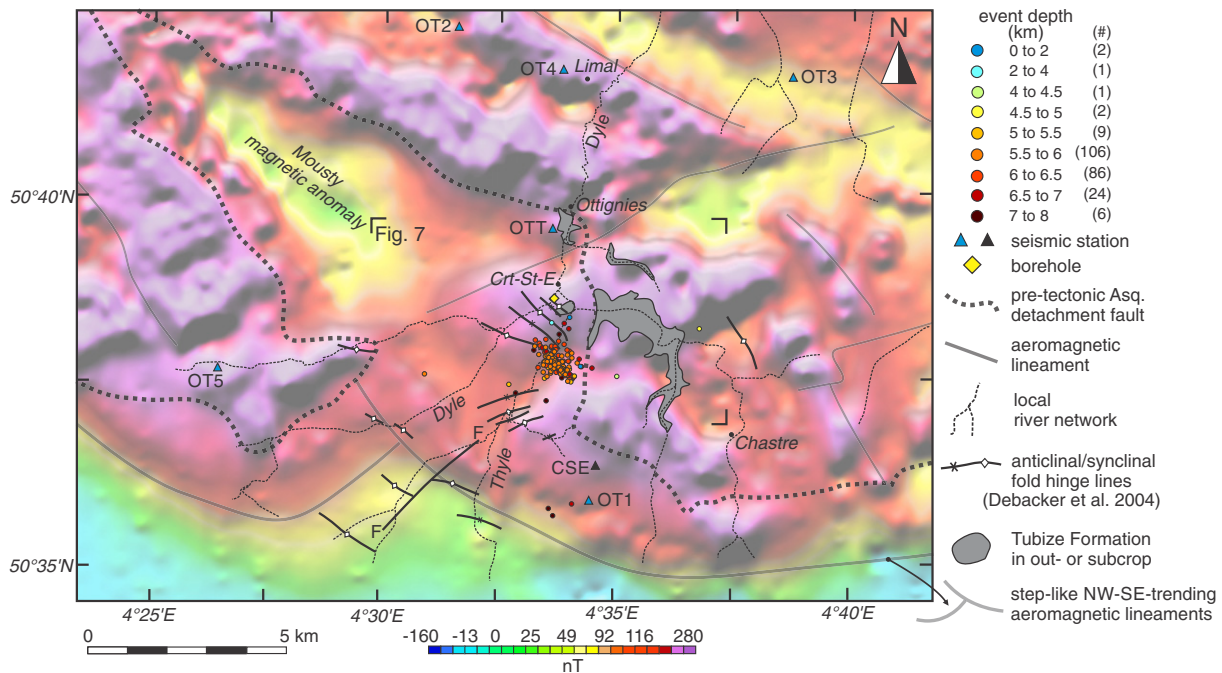


**Fig. 13.** Total magnetic field reduced-to-the-pole. Aeromagnetic highs correspond to shallowing of the magnetic Tubize Formation. Northwest of the seismic swarm, a magnetic trough coincides with a thick sequence of the low-magnetic pelitic Mousty Formation. The trough is bordered by a steep magnetic lineament to the north. The pre-cleavage, pre-folding Asquempont detachment fault (cf. Debacker et al., 2004a, see Fig. 2a) is located via the edges of magnetic highs. The 2008–2010 seismic swarm is situated between an ENE–WSW and a NW–SE-trending magnetic ridge. Crt-St-E: Court-Saint-Etienne. Original total field aeromagnetic data from Belgian Geological Survey (1994).

thus the separation of Mousty and Tubize, follows steep aeromagnetic gradients north and south of the Mousty aeromagnetic low (Fig. 13). The lineaments confirm the observations of boreholes that bedding at depth is steeply dipping in this area and presumably is situated within a high-strain shear zone (Debacker, 2012; Debacker et al., 2004a; Sintubin, 1997). These shear zones have never been observed at the surface, but the rapid transition between gently plunging and steeply plunging higher-order folds that are observed at the surface and which coincide with a pronounced magnetic anomaly gradients is interpreted to be the surface expression of these inferred shear zones.

The observed magnetic field anomaly is composed of signals that reflect the integrated effects of geological features of different sizes at different depths. The precise depth of a given magnetic anomaly cannot be uniquely determined. However, it is possible through filtering approaches to estimate magnetic anomalies that are likely to be associated with a given depth. Everaerts et al. (1996) and Sintubin and Everaerts (2002) briefly compared the differences between the ‘residual’ high-frequency and the ‘regional’ low-frequency aeromagnetic signal for the whole Brabant Massif by arbitrarily choosing a limit of a wavelength of 5 km to filter for shallow and deep structures. In both cases, the strong superposition of lineaments exists, suggestive of predominantly near-vertical attitudes in the slate belt. However, their arbitrarily chosen filter cannot definitively account for the anomalies associated specifically with depths of the seismic swarm.

## 5.2. Methodology of bandpass filtering

Aeromagnetic data have been proven to be very useful in providing information that links seismicity and deep-seated tectonic structures (e.g. Blakely et al., 2002; Shah et al., 2015). In order to separate short-wavelength anomalies that originate from shallow depths from long-wavelength anomalies that typically originate at greater depths, matched bandpass filtering may be used (Phillips, 1997, 2001). The methodology of the matched filtering approach works as follows: first the amplitude power spectra of the observed anomalies are calculated in the Fourier domain. Characteristically, the log power spectrum may have natural breaks between ranges of frequencies that correspond to different depth ranges representing geological layers (Phillips, 2001). Matched bandpass filters using sections of the power spectra separated at these natural breaks (Fig. 14a) can then be applied to decompose the observed magnetic anomaly (Fig. 14b). The resulting magnetic anomalies then highlight the sources at corresponding “equivalent” depths that are indicated by the natural breaks. For the area of investigation, the frequency–amplitude function was fitted with straight-line segments across the aeromagnetic RTP map until natural breaks that represent a source depth range corresponding to the depth of interest, i.e. in this study the hypocentre depths of the seismic swarm, were found.

We note that whilst this method can effectively separate magnetic layers, it cannot uniquely filter anomalies due to sources at specific depths. Whereas deep sources cannot generate short wavelengths, wide shallow sources with uniform magnetic properties can sometimes generate longer wavelengths that not necessarily represent deeper sources. However, shallow, gently-dipping structures are unlikely to occur in the study area; after all, outcrop studies and boreholes clearly indicate a steep lithological contact between the Mousty and Tubize Formations near Court-Saint-Etienne and the abundant presence of steeply dipping fold hinges (Fig. 7). Moreover, throughout the Cambrian core of the Brabant Massif, Legrand (1968) described many shallow boreholes and indicated that bedding in the Lower Cambrian formations is predominantly vertical.

Two sets of bandpass filters were considered, one which corresponds to layers centred at depths of approximately 45 m, 90 m, 0.47 km, 1.1 km, and 4.5 km (Filter 1, Table 4), and a second corresponding to depths of 47 m, 0.2 km, 0.55 km, 2.1 km, and 7.2 km (Filter 2, Table 4). For both sets, the deepest “layers” represent a halfspace and

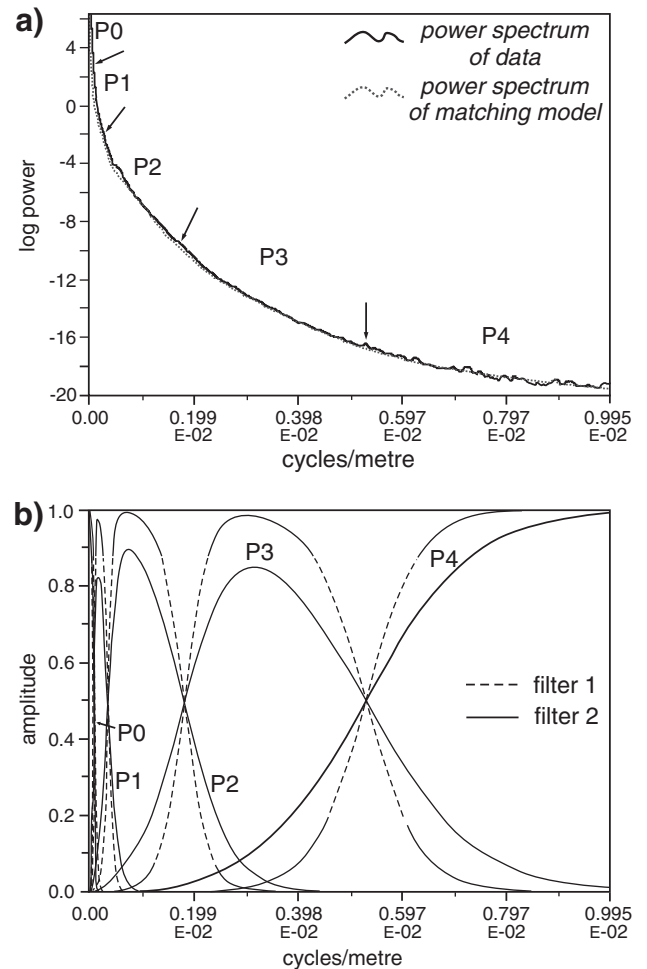


**Fig. 14.** Matched filtering decomposition of total-field aeromagnetic data. Equivalent depths are determined by fitting straight lines to the power spectrum (Phillips, 1997, 2001). a) Power spectrum of the chosen line segments (black line) and the matching five-layer equivalent model (dashed line). The different breaks along the power spectrum are carefully chosen as they allow filtering for depths of the seismic swarm. b) Magnetic field is decomposed into five components (P0 to P4). P1–P4 represent short- to medium-wavelength layers. P0 represents half-space long-wavelengths and results after lowpass filtering. Filter 1 filters to 4.4 km depth; filter 2 to 7.1 km depth (see also Table 4).

result from lowpass filtering. Magnetic anomaly maps corresponding to depths shallower than 1 km generally represent survey noise, aliasing artefacts (noting north–south survey flight line spacing of 0.5 km), and ringing from deeper sources. These maps were not used for interpretation and thus are not presented in Fig. 15. For the interpretation of depths deeper than 1 km, the flight height of 120 m needs to be included in the filtered depth resulting in depths corresponding to approximately 1.1 km, 2.0 km, 4.4 km and 7.1 km (Table 4). The effect of filtering is highlighted in cross-section A–A’ and B–B’ through the different generated maps (Figs. 15 and 16).

## 5.3. Interpretation of aeromagnetic bandpass filtered maps

### 5.3.1. Observations from the 1.1 km and 2.0 km maps

Many of the aeromagnetic lineaments deduced from the RTP map (Fig. 13) persist to equivalent depths of 1.1 km (Fig. 15a) and 2.0 km (Fig. 15b). There is a clear persistence of the Mousty magnetic anomaly, the NW–SE trending highs, the Asquempont detachment fault and the southern dextral shear zones from the surface to a depth of 2.0 km. This persistence suggests a steep attitude of these features. Furthermore, the similarity between the ENE–WSW and NW–SE orientation of the surface folds mapped by Debacker et al. (2004a) and the ENE–

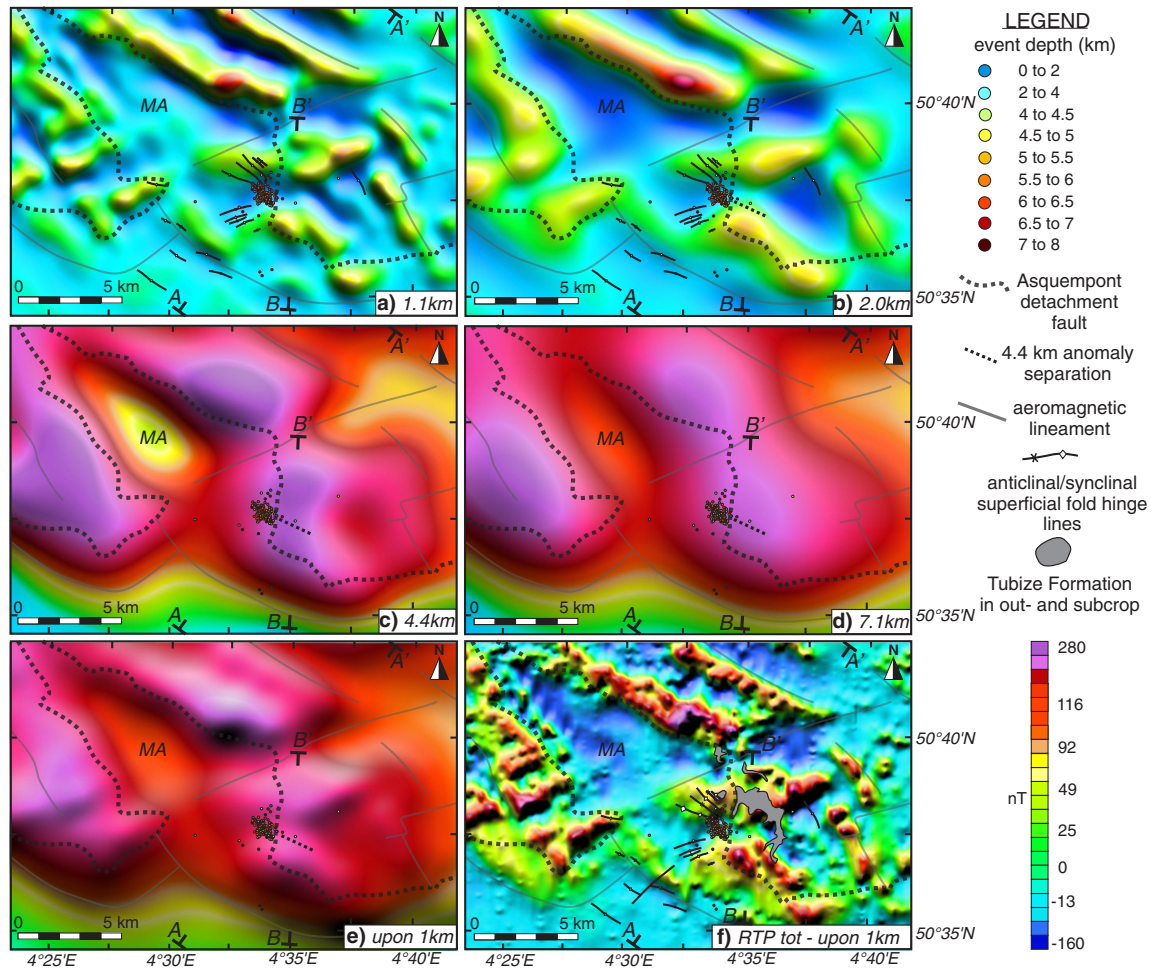


**Fig. 15.** Results of total magnetic intensity (RTP) matched filtering. MA: Mousty anomaly. a–b) Bandpass filtering for equivalent depths of 1.1 and 2.0 km. Note the pronounced similarity between the WNW–ESE and ENE–WSW oriented folds, respectively NW and SE of the seismic swarm, and the orientation of the magnetic anomaly in the subsurface. The swarm is situated between an E–W oriented magnetic ridge and the northwestern end of a NW–SE oriented ridge. The trace of the detachment fault remains persistent at depth. c–d) Bandpass filtering for equivalent depths of 4.4 and 7.1 km. The trace of the detachment fault persists to 4.4 km and 7.1 km. The swarm is situated east of a positive magnetic anomaly that is present as a single anomaly at 7.1 km but as two anomalies at 4.4 km. Note the dashed line as the separation of the positive magnetic anomaly at 4.4 km (Fig. 16 B–B'). The 2008–2010 hypocentres are situated approximately aligned with this separation. e) Total magnetic field RTP, lowpass filtered using an upward continuation distance of 1 km, highlighting deeper sources. f) Subtraction of the 1 km upward anomaly in e) from the total magnetic field RTP emphasises shallower sources.

WSW and NW–SE orientation of the magnetic highs at equivalent depths of 1.1 km and 2.0 km shows that the structural style and the variation of first-order folds persist to this depth.

The anomalies filtered for equivalent depths of 1.1 km and 2.0 km show magnetic sources associated with the geological structure above the seismic swarm. On these maps, the geology above the seismic swarm coincides with a negative magnetic anomaly representative of the Mousty slates and its structure is approximately aligned with the structural style marked by the NW–SE trending folds to the northwest. The negative anomaly east of the swarm corresponds to the presence of the low-magnetic quartzites of the Blanmont Formation (see Fig. 7 for the distribution of the Blanmont Formation).

### 5.3.2. Observations from the 4.4 km and 7.1 km maps

The anomaly maps filtered for equivalent depths of 4.4 km and 7.1 km roughly represent the magnetic sources of the top and the bottom of the 2008–2010 seismicity, respectively. Detailed observations at the size of the seismic swarm (1.5 km length) cannot be made due to the large filtered wavelengths (see wavelength versus size of the swarm in Fig. 16). Nonetheless, some interesting observations can be made: the Mousty anomaly and Asquepont detachment persistent to depths of 4.4 km and 7.1 km. At 7.1 km, the orientation of the Asquepont

detachment north of the Mousty anomaly is slightly different ( $N330^\circ$ ) than the trace deduced from the RTP anomaly map ( $N315^\circ$ ). With the exception of the dominant NW–SE oriented magnetic lineaments, other aeromagnetic lineaments deduced from the RTP anomaly map do not seem to persist to a depth of 7.1 km, or might not be resolvable given their size and the strong attenuation with depth in the magnetic data.

The southeastern end of the seismic swarm is coincident with a NNW–SSE oriented western edge of a positive magnetic anomaly (Fig. 15d). On the 7.1 km map, this magnetic anomaly has only one apparent source because of its large wavelength. However, various cross-sections (e.g. cross-section B–B' in Fig. 16) through these anomalies from the 4.4 km and the 1 km-upward maps (Fig. 15e; see further) suggest that the anomaly observed at 7.1 km can be separated into two individual sources with a NW–SE and WSW–ENE oriented attitude for the northern and southern anomaly, respectively. These anomalies also coincide with the orientation of anomalies observed at the 2.0 km map. The anomaly gradient that separates these two anomalies has a NW–SE orientation (indicated as a dashed black line in Fig. 15b–e) and is situated slightly north of the southeastern tip of the seismic swarm. This orientation has been detected by evaluating several N–S cross-sections through these magnetic highs. On the 2.0 km map, this

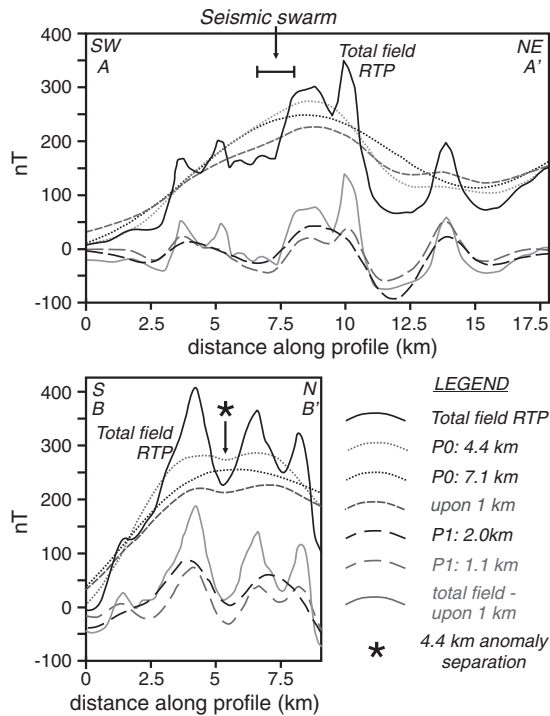


**Fig. 16.** Magnetic anomaly variation along profiles A–A' and B–B' for all filtered depths in Fig. 15. The RTP field is separated into different components. The seismic swarm is located at the southwest edge of a positive magnetic anomaly. The separation of the positive magnetic anomaly at 4.4 km in profile B–B' corresponds to the dashed line in Fig. 15.

anomaly coincides with the northern edge of the NW–SE oriented anomaly that is situated southeast of the swarm.

### 5.3.3. Shallow magnetic sources

To enhance anomalies due to shallow sources, an upward continuation strategy was chosen. The upward continued field shows what the magnetic anomaly would look like if the sensor had flown 1 km higher during survey effectively removing shorter wavelengths. The resulting anomaly reflects deeper sources as can be seen by the similarity between the 4.4 km map (Fig. 15c) and the 1 km-upward continued map (Fig. 15e). An anomaly associated with shallow sources can then be generated by subtracting the RTP upward continued anomaly from the total magnetic intensity aeromagnetic field. The resulting map is much better suited towards interpretation of shallow geological structures. Local magnetic variations are apparent after applying the upwards strategy and more strongly correspond to higher-order fold styles mapped at the surface (Fig. 15f) than do the matched-filtered maps in Fig. 15a and b.

## 6. Discussion

In literature seismic swarm occurrences are commonly related to fluid- or gas migration in the crust. This association relies both on the direct observation of hot springs and fluid- or gas outflow at the surface accompanying the swarm and on the observation of well-defined depth-related migration of seismicity (e.g. Daniel et al., 2011; Fischer et al., 2014; Lindenfeld et al., 2012; Schenk et al., 2012). According to the study of seismic swarms, triggering of seismicity by fluid overpressure at depth is often explained to be a likely cause (Fischer et al., 2014). In this section, however, we discuss that the 2008–2010 seismic swarm in the Brabant Massif is likely not affected by any fluid migration, nor that any overpressure needed to be present to have caused the two year activity along the causative fault. Reactivation of the causative fault by local stress conditions is a more likely hypothesis.

### 6.1. Stress release along a limited-sized fault

Unlike the fluid- or gas related swarm examples, 3D hypocentre distribution of the Walloon Brabant swarm does not show depth-related migration with time, supporting an alternative cause of seismicity. The seismic activity was restricted to a fault length of 1.5 km in a narrow ~200 m wide rock volume, and repetitively covered the entire zone. The Spring 2009 events, for example, all took place in the same area as the initiation of the swarm in August–September 2008. Consequently, within the hypocentral distribution, no relationship between the time history of events and a direction in rupture propagation is present. As

- (i) the seismic swarm is restricted to a rather small volume,
- (ii) seismic energy is released over large time span of 2 years within the same volume,
- (iii) no significant rupture propagation direction is deduced,

earthquake stress release is likely related to a heterogeneous stress field in a weakened crust. This indicates that the earthquakes in the seismic swarm do not correspond to the opening of a new structure but to the minor reactivation of a weakened and pre-existing, well-developed blind single fault structure that slowly released its energy in response to the current stress field. The incapability to build up high stress accumulations is reflected in the low *b*-value of the 2008–2010 catalogue. Given their small magnitudes and the consistent focal mechanisms, the earthquakes thus reflect millimetre to centimetre displacements along the fault plane.

Due to the small size of the swarm relative to its depth, a specific fault structure cannot be easily visualised by matched filtering of the magnetic anomaly. However, as matched filtering is consistent with superficial structures deduced from field mapping and confirms that the steep bedding attitude of Lower Cambrian deposits encountered in boreholes and at the surface persist to large depths (cf. Sintubin and Everaerts, 2002), the significance of the causative structure responsible for the near-vertical 2008–2010 Walloon Brabant seismic can be deduced by interpreting the different filtered maps. Given this verticality, the tectonic structure observed from the 2.0 km map (Fig. 15b) can be used to explain the seismic swarm. At both ends, the fault structure associated with the 2008–2010 earthquake seismicity in Walloon Brabant seems to be confined by magnetic sources that have a different orientation than the orientation of the seismic swarm (Fig. 15). The northwestern tip of the swarm does not extend into the ENE–WSW magnetic anomaly high (Fig. 15b), whereas its southeastern tip terminates near a NW–SE oriented positive anomaly that is visible in the 2.0 km (Fig. 15b), 4.1 km (Fig. 15c) and 7.1 km maps (Fig. 15e). The fact that the locally N–S-trending Asquemont detachment fault is consistently present near the southeastern end of the swarm at the discussed depths strongly suggests that the southeastern part of the causative fault structure is confined by a density and rheological contrast that exists between the slates of the Mousty Formation and the metasandstones of the Tubize Formation. Consequently, assuming that the structures are indeed nearly vertical, the steeply-dipping Asquemont detachment fault, illuminated by a magnetic gradient at 2.0 km, 4.4 km and 7.1 km depth, demonstrates a geological contrast in rock formations that can be considered to have limited the seismic swarm activity (Fig. 17). These findings indicate a NW–SE trending causative fault structure that is only situated in the Mousty slates and which is limited in length as it probably does not exist in the footwall of the detachment fault in the Tubize Formation. Matched filtering thus strongly suggests that the limited spatial extent of the seismic swarm is due to limited length of the corresponding fault.

We also speculate that the 1953–1957 seismicity, which included events with slightly larger magnitudes, resulted from the activity along the same fault although at that time it was capable of releasing more seismic energy than the 2008–2010 seismicity. If all the

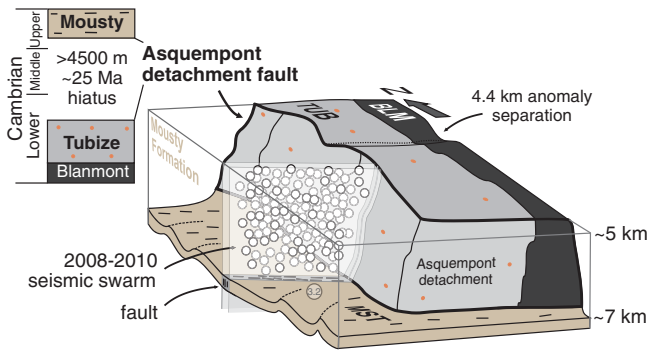


**Fig. 17.** Schematic 3D representation summarising the geology in the hypocentre area of the 2008–2010 seismic swarm in the Brabant Massif. Seismicity took place between 5 and 7 km within the slaty Mousty Formation along a limited-sized, NW–SE oriented fault that is bordered at its southeastern end by the early-orogenic, steeply-dipping and folded Asquempont detachment fault. In the hypocentre area, this detachment fault separates the highly magnetised Tubize Formation from the younger, poorly magnetised slaty Mousty Formation. Local fold variations in the Mousty Formation are projected from surface geological maps (Debacker et al., 2004a). Figure not to scale.

cumulative energy of the 2008–2010 swarm would have been released at the same time, it would have generated a  $M_L$  3.9 event, i.e. comparable to the total moment release of the  $M_L$  4.0 event in 1953. However, considering all the events of the 1953–1957 swarm (Table 3), the total moment release of the 1953–1957 swarm is larger than the total 2008–2010 swarm. It remains an open question whether or not the 51-year time gap between the 1953–1957 and 2008–2010 seismic swarms can be interpreted as a seismic cycle.

## 6.2. Seismotectonic interpretation

Earthquake analysis of events that occurred at the many normal faults bordering the Lower Rhine Embayment (LRE; Fig. 2c, Fig. 11c), i.e. the closest active regional structure that forms the northwestern relay of the Rhine Graben, indicates a current extensional regional stress regime (Camelbeeck and van Eck, 1994; Camelbeeck et al., 2007; Hinzen, 2003; Hinzen and Reamer, 2007; Reamer and Hinzen, 2004; Vanneste et al., 2013). The NW–SE-directed maximum horizontal stress ( $\sigma_H$ ; Fig. 11c) defined from the inversion of focal mechanisms of these earthquakes agrees well with the seismotectonic model of NW Europe (Ahorner, 1975, 1985) and the World Stress Map (Zoback, 1992) showing that the regional stress of the LRE is controlled by plate driving forces acting on plate boundaries.

The stress field inferred from inversion of focal mechanisms of the Walloon Brabant seismic swarm, however, resulted in a local stress field with a WNW–ESE maximum horizontal stress ( $\sigma_H = N289^\circ$ ; Fig. 11b) which differs and deviates from the regional trend ( $\sigma_H = N312^\circ$ ; Hinzen, 2003). To evaluate our obtained stress inversion and to derive a local stress field orientation for the studied part of the Brabant Massif, we need to compare the focal mechanisms of the 2008–2010 seismic swarm with the focal mechanisms of other seismic events. Unfortunately, apart from the seismic swarm, the studied region has limited historical seismic activity. Only one focal mechanism, the 1995  $M_L$  4.5 Le Roeulx earthquake (35 km WSW of the seismic swarm, Fig. 2c), can be compared with that of the seismic swarm. This earthquake occurred at a depth of 24 km, considerably deeper than the 2008–2010 swarm, and is interpreted to have occurred along the southern border of the Brabant Massif. Its mechanism is reverse along a steeply dipping NNE–SSW trending fault (Camelbeeck, 1993; Camelbeeck et al., 2007). Aftershocks are unfortunately lacking and a reliable stress field cannot be calculated from this one event.

Another significant earthquake in the Brabant Massif is the damaging  $M_s$  5.0 1938 earthquake (75 km WNW of the swarm, Fig. 2c) and its two  $M_L > 4.0$  aftershocks. No reliable fault-plane solution is available

due to a lack of seismic data for the time (Camelbeeck et al., 2007). Predominantly E–W oriented isoseismals from this event have been deduced from historical documents (Somville, 1939), which led Ahorner (1975) to conclude that this event resulted from strike-slip faulting along a WNW–ENE-trending shear zone. Nguyen et al. (2004), however, suggested that the E–W oriented isoseismals are related to regional site effects in the 1938 epicentre area rather than to the mechanism of faulting.

The only independent method that can be used to evaluate the derived local stress field is calculation of the spatial variation of the differences in gravitational potential energy from the method of Camelbeeck et al. (2013). This method shows that local depth-integrated stress sources can be inferred from the second spatial derivative of the geoid height, which is used as a proxy for the gravitational potential energy. The inversion of the geoid height applied to Belgium is indicated in Fig. 11c. As only local differences in the gravitational potential energy are applied, the resulting stress tensor is also local. Interestingly, the applied geoid method shows a local stress field with a WNW–ESE  $\sigma_H$  direction in the 2008–2010 epicentral area. This similarity of the geoid independent stress tensor ( $N280^\circ$ ; Fig. 11c) and the stress field inferred from inversion of the ten calculated focal mechanisms ( $N289^\circ$ ; Fig. 11b) suggest that our strike-slip stress tensor is reliable, even when considering the uncertainty of  $30^\circ$  of the local stress tensor given by the Win-Tensor programme.

When considering the uncertainty in the estimation of the local stress field (error of  $30^\circ$ , Fig. 11c) with the regional stress tensor, there is only a small overlap between both stress tensors but the mechanisms are different (strike-slip versus extensional; Fig. 11c). Stress inversion carried out in this study thus shows for the first time that a local left-lateral strike-slip regime is currently present within the studied southern part of the Brabant Massif and that the local stress configuration was presumably the main driver of the 2008–2010 seismicity.

## 6.3. General implications for intraplate earthquake activity

The geometry of the 2008–2010 seismic activity indicates an active fragmented fault structure within the Caledonian Brabant Massif. Also other kilometre-long, NW–SE aeromagnetic lineaments are present in the southern part of the Brabant Massif (Fig. 2c). Due to their NW–SE orientation these lineaments might have a similar reactivation potential in the current stress field as the causative structure of the 2008–2010 seismicity. The limited size of the causative fault studied in this work however suggests that such long lineaments may be more fragmented than previously thought and that they thus may have a lower potential to generate large earthquakes in an intraplate setting as their full length cannot be considered. To investigate this statement, magnetic lineaments that highlight fault structures in old geological massifs need to be studied in more detail by the aeromagnetic methods presented in this paper. This will reveal their continuation at depth and their reactivation potential, even though no seismicity has taken place along them in the past.

## 7. Conclusions

A comprehensive seismological and seismotectonic analysis of the 2008–2010 earthquake swarm that took place near the city of Court-Saint-Etienne (Belgium) within the basement rocks of the Anglo-Brabant Massif, and multidisciplinary analysis of the available seismological, geological and potential geophysical data emphasise the importance of inherited fault structures and their reactivation potential in an intraplate seismotectonic setting. In particular:

- 1) Application of seldomly-used cross-correlation tools resulted in significant refinement of the first P-wave arrival times. Relocation in HypoDD showed that the original locations of the 2008–2010 seismic events can be improved to a fault structure that is limited

to a horizontal length of 1.5 km and width of ~200 m, and is restricted in the vertical direction between 5 and 7 km depth. The analysis of time history of events shows that the swarm occurred in several bursts of activity, with dominant phases in the summer and autumn of 2008 and in the spring of 2009. Neither depth migration, nor any horizontal rupture propagation can be demonstrated by the time occurrence of events. This indicates a rather slow and diffuse energy release during the two year swarm activity. The low *b*-value of the seismic catalogue indicates a dominance of small events over large events in a magnitude range between  $M_L$  0.4 and  $M_L$  3.2.

- 2) Comparison between the NW–SE oriented epicentral distribution and the fault plane solution of the largest events shows that the NW–SE nodal plane can be interpreted as the true fault plane. The focal mechanisms of ten events define left-lateral oblique to purely left-lateral strike-slip movements on a subvertical fault structure.
- 3) The waveform of the 1953  $M_L$  4.0 seismic event that took place near the 2008–2010 epicentral area shows a pronounced similarity in the asymmetry of the first S-wave arrival compared to the largest events of the 2008–2010 seismic swarm. Based on this comparison we speculate that the 1953–1957 events may have occurred along the same fault structure.
- 4) To find a relevant tectonic structure that may correspond to the seismic swarm, we applied a systematic filtering approach in which the magnetic field was bandpass matched-filtered to generate magnetic anomaly maps that highlight sources at equivalent depths. Filtering results and their comparison to the local geological structure strongly suggest that the causative fault is situated in a slaty rock body and is bordered at its both ends by magnetic anomalies with significant different orientations representing a different and stronger rock type. This analysis suggests that the fault along which seismicity took place is an isolated structure with an orientation that is consistent with the structural grain of this part of the Brabant Massif and that the limited spatial extent of the seismic swarm is due to limited length of the corresponding fault.
- 5) Stress inversion of the focal mechanisms indicates a local strike-slip stress regime with a WNW–ESE oriented maximum horizontal stress orientation. This local WNW–ESE stress orientation agrees with the local stress orientation independently inferred from the second spatial derivative of the geoid height and differs slightly from estimates of the regional stress field. Based on this comparison, local stresses are likely the cause of the seismicity.

## Acknowledgements

The authors would like to acknowledge B. Lamarche (OTT), G. Wyseur (OT1), M. Gosuin (OT2), M. Piaser (OT3), K. de Wit (OT4), J.-P. Deckens (OT5) and P. Paquet (GRZ) for housing the temporary seismic stations. G. Rapagnani, F. Colin, L. Vandercoilden and B. Bukasa are thanked for station maintenance during the seismic swarm. H. Martin is thanked for the focal mechanism calculation in the DP console available at the Royal Observatory of Belgium. We are grateful to F. Waldhauser for the HypoDD2+ *beta* version and to L. Krischer (HypoDDpy), K. Vanneste and B. Vleminckx for their help with python script development. We very much appreciate the fruitful discussions with T.N. Debacker, A. Herbosch, M. Sintubin, K. Verbeeck and J. Phillips on the aeromagnetism of the Brabant Massif. Constructive remarks of V.E. Langenheim, N. Woodcock, an anonymous reviewer, M. Van Camp and editor K. Wang greatly helped to improve the manuscript. The DEM model in Figs. 3 and 7 is published with authorisation A3134 of the Nationaal Geografisch Instituut. The aeromagnetic raw data in the online supplementary data are released after approval of the Belgian Geological Survey. This research was funded by BELSPO (project MO-33-028) and Fonds de la Recherche Scientifique - FNRS under grant F6/15-MCF/OL. K. Van Noten additionally benefited from a travel funding of the Fonds voor Wetenschappelijk Onderzoek Vlaanderen (FWO) to attend AGU2013. Relocation tools were developed during

the FRIA scholarship FC76908 of T. Lecocq. Any use of trade names is for descriptive purposes only and does not imply endorsement by the U.S. Government.

## Appendix. Supplementary data

Supplementary data associated with this article can be found in the online version, at <http://dx.doi.org/10.1016/j.tecto.2015.05.026>. These data include the seismic catalogue of relocated events, raw magnetic flight line data and the Google Earth map of the most important areas described in this article.

## References

- Ahorner, L., 1975. Present-day stress field and seismotectonic block movements along major fault zones in Central Europe. *Tectonophysics* 29, 233–249.
- Ahorner, L., 1985. The general pattern of seismotectonic dislocations in Central Europe as the background for the Liège earthquake on November 8, 1983. In: Melchior, P. (Ed.), *Seismic Activity in Western Europe*. Springer Netherlands, pp. 41–56.
- Angelier, J., Mechler, P., 1977. Sur une méthode graphique de recherche des contraintes principales également utilisable en tectonique et en séismologie: la méthode des dièdres droits. *Bull. Soc. Geol. Fr.* (19), 1309–1318.
- Barani, S., Ferretti, G., Scafidi, D., Spallarossa, D., 2014. Analysis of seismicity and micro-seismicity associated with the October–November 2010 Sampeyre swarm, Southwestern Alps. *Tectonophysics* 611, 130–140.
- Belgian Geological Survey, 1994. Aeromagnetic map of the Brabant Massif: residual total field reduced to the pole. 1:100 000.
- Beyreuther, M., Barsch, R., Krischer, L., Megies, T., Behr, Y., Wassermann, J., 2010. ObsPy: a python toolbox for seismology. *SRL* 81, 530–533.
- Blakely, R.J., Wells, R.E., Weaver, C.S., Johnson, S.Y., 2002. Location, structure, and seismicity of the Seattle fault zone, Washington: evidence from aeromagnetic anomalies, geologic mapping, and seismic-reflection data. *GSA Bull.* 114, 169–177.
- Bott, M.P.H., 1959. The mechanics of oblique-slip faulting. *Geol. Mag.* 96, 109–117.
- Camelbeek, T., 1993. Mécanisme au foyer des tremblements de terre et contraintes tectoniques: le cas de la zone intraplaque belge. Université Catholique de Louvain, Louvain-la-Neuve (PhD Thesis, 344 pp.).
- Camelbeek, T., van Eck, T., 1994. The Roer Valley Graben earthquake of 13 April 1992 and its seismotectonic setting. *Terra Nova* 6, 291–300.
- Camelbeek, T., Vanneste, K., Alexandre, P., Verbeeck, K., Petermans, T., Rosset, P., Everaerts, M., Warnant, R., Van Camp, M., 2007. Relevance of active faulting and seismicity studies to assessments of long-term earthquake activity and maximum magnitude in intraplate northwest Europe, between the Lower Rhine Embayment and the North Sea. *Geol. Soc. Am. Spec. Pap.* 425, 193–224.
- Camelbeek, T., de Viron, O., Van Camp, M., Kusters, D., 2013. Local stress sources in Western Europe lithosphere from geoid anomalies. *Lithosphere* 5, 235–246.
- Camelbeek, T., Alexandre, P., Sabbe, A., Knuts, E., Garcia Moreno, D., Lecocq, T., 2014. The impact of the earthquake activity in Western Europe from the historical and architectural heritage records. In: Talwani, P. (Ed.), *Intraplate Earthquakes*. Cambridge University Press, pp. 198–230.
- Chacksfield, B.C., De Vos, W., D'Hooge, L., Duser, M., Lee, M.K., Poitevin, C., Royles, C.P., Verniers, J., 1993. A new look at Belgian aeromagnetic and gravity data through image-based display and integrated modelling techniques. *Geol. Mag.* 130, 583–591.
- Charlier, C., Van Gils, J., 1953. Liste des stations sismologiques mondiales. L'association internationale de séismologie, Observatoire Royal de Belgique (282 pp.).
- Daniel, G., Prono, E., Renard, F., Thouvenot, F., Hainzl, S., Marsan, D., Helmstetter, A., Traversa, P., Got, J.L., Jenatton, L., Guiguet, R., 2011. Changes in effective stress during the 2003–2004 Ubaye seismic swarm, France. *J. Geophys. Res. Solid Earth* 116, B01309.
- de Magnée, I., Raynaud, J., 1944. Etude magnétique de la tectonique du Cambrien du Brabant à l'est de Court-St-Etienne. *Ann. Soc. Geol. Belg.* 67, 495–546.
- De Vos, W., Poot, B., Hus, J., El Khayati, M., 1992. Geophysical characterization of lithologies from the Brabant Massif as a contribution to gravimetric and magnetic modelling. *Soc. Belge Géol. Bull.* 101, 173–180.
- De Vos, W., Herbosch, A., Vanguestaine, M., 1993a. A new geological map of the Brabant Massif, Belgium. *Geol. Mag.* 130, 605–611.
- De Vos, W., Chacksfield, B.C., D'Hooge, L., Duser, M., Lee, M.K., Poitevin, C., Royles, C.P., Vandenborgh, J., Van Eyck, J., Verniers, J., 1993b. Image-based display of Belgian digital aeromagnetic and gravity data. *Belgian Geological Survey Professional Paper* 263, pp. 1–20.
- Debacker, T.N., 2012. Folds and cleavage/folds relationships in the Brabant Massif, southeastern Anglo-Brabant Deformation Belt. *Geol. Belg.* 15, 81–95.
- Debacker, T.N., Herbosch, A., Sintubin, M., Verniers, J., 2003. Palaeozoic deformation history of the Asquempont–Virginal area (Brabant Massif, Belgium): large-scale slumping, low-angle extensional detachment development (the Asquempont Fault redefined) and normal faulting (the Nieuwpoort–Asquempont fault zone). *Geol. Surv. Belg. Mem.* 49, 1–30.
- Debacker, T.N., Herbosch, A., Sintubin, M., 2004a. The supposed thrust fault in the Dyle–Thyle outcrop area (southern Brabant Massif, Belgium) re-interpreted as a folded low-angle extensional detachment. *Geol. Belg.* 8, 53–69.
- Debacker, T.N., Sintubin, M., Verniers, J., 2004b. Transitional geometries between gently plunging and steeply plunging folds: an example from the Lower Paleozoic Brabant Massif, Anglo-Brabant deformation belt, Belgium. *J. Geol. Soc. Lond.* 161, 641–652.

- Debacker, T.N., Dewaele, S., Sintubin, M., Verniers, J., Muchez, P., Boven, A., 2005. Timing and duration of the progressive deformation of the Brabant Massif, Belgium. *Geol. Belg.* 8, 20–34.
- Debacker, T.N., Sintubin, M., Robion, P., 2010. On the use of magnetic techniques for stratigraphic purposes: examples from the Lower Palaeozoic Anglo-Brabant Deformation Belt (Belgium). *Geol. Belg.* 13, 333–350.
- Deichmann, N., Garcia-Fernandez, M., 1992. Rupture geometry from high-precision relative hypocentre locations of microearthquake clusters. *Geophys. J. Int.* 110, 501–517.
- Delcambre, B., Pingot, J.-L., 2002. Carte Chastre-Gembloux n° 40/5-6, Carte géologique de la Wallonie, échelle 1/25000. Ministère de la Région Wallonne, Namur.
- Delvaux, D., Sperner, B., 2003. Stress tensor inversion from fault kinematic indicators and focal mechanism data: the TENSOR program. In: Nieuwland, D. (Ed.), *New Insights Into Structural Interpretation and Modelling*. Geological Society, London, Special Publications 212, pp. 75–100.
- Everaerts, M., 2000. L'interprétation structurale de la Manche au Rhin: apport du filtrage des champs de potentiel. Université Catholique de Louvain, p. 167.
- Everaerts, M., De Vos, W., 2012. Gravity acquisition in Belgium and the resulting Bouguer anomaly map, Memoirs of the Geological Survey of Belgium. Koninklijk Belgisch Instituut voor Natuurwetenschappen. Belgische Geologische Dienst, Brussels, p. 39.
- Everaerts, M., Poitevin, C., De Vos, W., Sterpin, M., 1996. Integrated geophysical/geological modelling of the Western Brabant Massif and structural implications. *Soc. Belge Géol. Bull.* 105, 41–59.
- Fischer, T., Horálek, J., Hrubcová, P., Vavryčuk, V., Bräuer, K., Kämpf, H., 2014. Intra-continental earthquake swarms in West-Bohemia and Vogtland: a review. *Tectonophysics* 611, 1–27.
- Gutenberg, B., Richter, C.F., 1956. Earthquake magnitude, intensity, energy and acceleration. *Bull. Seismol. Soc. Am.* 46, 105–145.
- Hainzl, S., 2004. Seismicity patterns of earthquake swarms due to fluid intrusion and stress triggering. *Geophys. J. Int.* 159, 1090–1096.
- Hainzl, S., Fischer, T., 2002. Indications for a successively triggered rupture growth underlying the 2000 earthquake swarm in Vogtland/NW Bohemia. *J. Geophys. Res.* 107, 2338.
- Herbosch, A., Verniers, J., 2013. Stratigraphy of the Lower Palaeozoic of the Brabant Massif, Belgium. Part I: the Cambro-Ordovician from the Halle and Ottignies groups. *Geol. Belg.* 16, 49–64.
- Hiemer, S., Toessler, D., Scherbaum, F., 2012. Monitoring the West Bohemian earthquake swarm in 2008/2009 by a temporary small-aperture seismic array. *J. Seismol.* 16, 169–182.
- Hinzen, K.-G., 2003. Stress field in the northern Rhine area, central Europe, from earthquake fault plane solutions. *Tectonophysics* 377, 325–356.
- Hinzen, K.-G., Reamer, S.K., 2007. Seismicity, seismotectonics, and seismic hazard in the Northern Rhine Area. In: Stein, S., Mazzotti, S. (Eds.), *Continental Intraplate Earthquakes: Science, Hazard, and Policy Issues* vol. Special Paper 425. Geological Society of America, pp. 225–242.
- Hofmann, R.B., 1996. Individual faults can't produce a Gutenberg–Richter earthquake recurrence. *Eng. Geol.* 43, 5–9.
- Ibs-von Seht, M., Plenefisch, T., Klinge, K., 2008. Earthquake swarms in continental rifts – a comparison of selected cases in America, Africa and Europe. *Tectonophysics* 452, 66–77.
- Krischer, L., 2015. hypoDDpy: hypoDDpy 1.0. Zenodo 10.5281/zenodo.18907.
- Leclère, H., Fabbri, O., Daniel, G., Cappa, F., 2012. Reactivation of a strike-slip fault by fluid overpressuring in the southwestern French–Italian Alps. *Geophys. J. Int.* 189, 29–37.
- Lecocq, T., 2011. L'activité sismique en Ardenne et sa relation avec la tectonique active, Département des Sciences de la Terre et de l'Environnement. Université Libre de Bruxelles, Brussels, p. 265 (PhD Thesis).
- Lecocq, T., Rapagnani, G., Martin, H., De Vos, F., Hendrickx, M., Van Camp, M., Vanneste, K., Camelbeeck, T., 2009. B-FEARS: The Belgian Felt Earthquake Alert and Report System. *Cahiers du Centre Européen de Géodynamique et de Séismologie*.
- Lee, W.H.K., Lahr, J.C., 1972. Hypo71: a computer program for determining hypocenter, magnitude, and first motion pattern of local earthquakes. *U.S. Geol. Surv. Open File Rep.* 72–223 (100 pp.).
- Lee, M.K., Pharaoh, T.C., Williamson, J.P., Green, C.A., De Vos, W., 1993. Evidence on the deep structure of the Anglo-Brabant Massif from gravity and magnetic data. *Geol. Mag.* 130, 575–582.
- Legrand, L., 1968. Le Massif du Brabant. Mémoires pour servir à l'explication des cartes géologiques et minières de la Belgique. Service Géologique de Belgique, Bruxelles.
- Leynaud, D., Jongmans, D., Teerlynck, H., Camelbeeck, T., 2000. Seismic hazard assessment in Belgium. *Geol. Belg.* 3, 67–86.
- Lindenfeld, M., Rumpker, G., Link, K., Koehn, D., Batte, A., 2012. Fluid-triggered earthquake swarms in the Rwenzori region, East African Rift—evidence for rift initiation. *Tectonophysics* 566–567, 95–104.
- Mansy, J.L., Everaerts, M., De Vos, W., 1999. Structural analysis of the adjacent Acadian and Variscan fold belts in Belgium and northern France from geophysical and geological evidence. *Tectonophysics* 309, 99–116.
- Melville, C., Levret, A., Alexandre, P., Lambert, J., Vogt, J., 1996. Historical seismicity of the Strait of Dover-Pas de Calais. *Terra Nova* 8, 626–647.
- Mogi, K., 1963. Some discussions on aftershocks, foreshocks and earthquake swarms—the fracture of a semi-infinite body caused by an inner stress origin and its relation to the earthquake phenomena. *Bull. Earthquake Res. Inst.* 41, 615–658.
- Nguyen, F., Van Rompaey, G., Teerlynck, H., Van Camp, M., Jongmans, D., Camelbeeck, T., 2004. Use of microtremor measurement for assessing site effects in Northern Belgium – interpretation of the observed intensity during the Ms = 5.0 June 11 1938 earthquake. *J. Seismol.* 8, 41–56.
- Parotidis, M., Rothert, E., Shapiro, S.A., 2003. Pore-pressure diffusion: a possible triggering mechanism for the earthquake swarms 2000 in Vogtland/NW-Bohemia, central Europe. *Geophys. Res. Lett.* 30, 1–4.
- Phillips, J.D., 1997. Potential-field Geophysical Software for the PC, Version 2.2 (<http://pubs.usgs.gov/of/1997/ofr-1997-0725/>), U.S. Geol. Surv. Open File Rep. 97–725 (34 pp.).
- Phillips, J.D., 2001. Designing matched bandpass and azimuthal filters for the separation of potential-field anomalies by source region and source type, Australian Society of Exploration Geophysicists. 15th Geophysical Conference and Exhibition, Expanded Abstracts CD-ROM (4 pp.).
- Piesens, K., Vancampenhout, P., De Vos, W., 2005. Geologische subcropkaart van het Massief van Brabant in Vlaanderen. Schaal 1:200.000. Opgemaakt door de BGD in opdracht van ANRE, Ministerie van de Vlaamse Gemeenschap, project VLA/03.1-1.
- Reamer, S.K., Hinzen, K.-G., 2004. An earthquake catalog for the Northern Rhine Area, Central Europe (1975–2002). *Seismol. Res. Lett.* 75, 713–725.
- Schaff, D.P., Waldhauser, F., 2005. Waveform cross-correlation-based differential travel-time measurements at the Northern California seismic network. *Bull. Seismol. Soc. Am.* 95, 2446–2461.
- Schenk, V., Schenková, Z., Jechumtálová, Z., Pichl, R., 2012. Crustal deformations in the epicentral area of West Bohemia 2008 earthquake swarm in central Europe. *J. Geophys. Res.* 117, 1–19.
- Scherbaum, F., 2001. *Of Poles and Zeros: Fundamentals of Digital Seismology*. Springer, Netherlands.
- Shah, A.K., Horton, J.W., Burton, W.C., Spears, D.B., Gilmer, A.K., 2015. Subsurface geologic features of the 2011 central Virginia earthquakes revealed by airborne geophysics. In: Horton, J.W., Chapman, M.C., Green, R.A. (Eds.), *The 2011 Mineral, Virginia Earthquake and Its Significance for Seismic Hazards in Eastern North America*. Geological Society of America Special Papers 509, pp. 295–304.
- Sibson, R., 1985. A note on fault reactivation. *J. Struct. Geol.* 7, 751–754.
- Sintubin, M., 1997. Structural implications of the aeromagnetic lineament geometry in the Lower Paleozoic Brabant Massif (Belgium). *Aardkundige Mededelingen*. 8 pp. 165–168.
- Sintubin, M., 1999. Arcuate fold and cleavage patterns in the southeastern part of the Anglo-Brabant fold Belt (Belgium): tectonic implications. *Tectonophysics* 309, 81–97.
- Sintubin, M., Everaerts, M., 2002. A compressional wedge model for the Lower Paleozoic Anglo-Brabant Belt (Belgium) based on potential field data. In: Winchester, J.A., Pharaoh, T., Verniers, J. (Eds.), *Paleozoic Amalgamation of Central Europe*. Geological Society, London, Special Publication, London, pp. 327–343.
- Sintubin, M., Debacker, T.N., Van Baelen, H., 2009. Early Paleozoic orogenic events north of the Rhenic suture (Brabant, Ardenne): a review. *Compt. Rendus Geosci.* 341, 156–173.
- Somville, O., 1939. Le tremblement de terre belge du 11 juin 1938. Publication de l'Observatoire Royal de Belgique, Imprimerie Duculot, Gembloux (16 pp.).
- Špičák, A., 2000. Earthquake swarms and accompanying phenomena in intraplate regions: a review. *Stud. Geophys. Geod.* 44, 89–106.
- Van Noten, K., Van Baelen, H., Sintubin, M., 2012. The complexity of 3D stress-state changes during compressional tectonic inversion at the onset of orogeny. In: Healy, D., Butler, R.W.H., Shipton, Z.K., Sibson, R.H. (Eds.), *Faulting, Fracturing, and Igneous Intrusion in the Earth's Crust*. Geological Society, London, Special Publications 367, pp. 51–69.
- Van Tassel, R., 1986. Contribution à la lithologie du segment Caledonien des vallées de la Dyle et de la Thyle, Brabant, Belgique. *Aardkundige Mededelingen*. 3 pp. 239–268.
- Vander Auwera, J., André, L., 1985. Sur le milieu de dépôt, l'origine des matériaux et le faciès métamorphique de l'Assise de Tubize (Massif du Brabant, Belgique). *Soc. Belge Géol. Bull.* 94, 171–184.
- Vanneste, K., Camelbeeck, T., Verbeeck, K., 2013. A model of composite seismic sources for the Lower Rhine Graben, Northwest Europe. *Bull. Seismol. Soc. Am.* 103, 984–1007.
- Verniers, J., Pharaoh, T.C., André, L., Debacker, T.N., De Vos, W., Everaerts, M., Herbosch, A., Samuelsson, J., Sintubin, M., Vecoli, M., 2002. The Cambrian to mid Devonian basin development and deformation history of eastern Avalonia, east of the Midlands Microcraton: new data and a review. In: Winchester, J.A., Pharaoh, T.C., Verniers, J. (Eds.), *Paleozoic Amalgamation of Central Europe*. Geological Society, London, Special Publications, pp. 49–93.
- Waldhauser, F., Ellsworth, W.L., 2000. A double-difference earthquake location algorithm: method and application to the Northern Hayward Fault, California. *Bull. Seismol. Soc. Am.* 90, 1353–1368.
- Wallace, R.E., 1951. Geometry of shearing stress and relation to faulting. *J. Geol.* 69, 118–130.
- Zoback, M.L., 1992. First- and second-order patterns of stress in the lithosphere: the world stress map project. *J. Geophys. Res.* 97, 11703–11728.